BAMS Article

An Operational Multi-Radar Multi-Sensor QPE System in Taiwan

Pao-Liang Chang, Jian Zhang, Yu-Shuang Tang, Lin Tang, Pin-Fang Lin, Carrie Langston, Brian Kaney, Chia-Rong Chen, and Kenneth Howard

ABSTRACT: Over the last two decades, the Central Weather Bureau of Taiwan and the U.S. National Severe Storms Laboratory have been involved in a research and development collaboration to improve the monitoring and prediction of river flooding, flash floods, debris flows, and severe storms for Taiwan. The collaboration resulted in the Quantitative Precipitation Estimation and Segregation Using Multiple Sensors (QPESUMS) system. The QPESUMS system integrates observations from multiple mixed-band weather radars, rain gauges, and numerical weather prediction model fields to produce high-resolution (1 km) and rapid-update (10 min) rainfall and severe storm monitoring and prediction products. The rainfall products are widely used by government agencies and emergency managers in Taiwan for flood and mudslide warnings as well as for water resource management. The 3D reflectivity mosaic and QPE products are also used in high-resolution radar data assimilation and for the verification of numerical weather prediction model forecasts. The system facilitated collaborations with academic communities for research and development of radar applications, including quantitative precipitation estimation and nowcasting. This paper provides an overview of the operational QPE capabilities in the Taiwan QPESUMS system.

KEYWORDS: Asia; Precipitation; Hydrometeorology; Data quality control; Radars/Radar observations; Remote sensing

https://doi.org/10.1175/BAMS-D-20-0043.1

Corresponding author: Jian Zhang, jian.zhang@noaa.gov

In final form 19 February 2020

AFFILIATIONS: Chang, Y.-S. Tang, Lin, and Chen—Central Weather Bureau, Taipei, Taiwan; **Zhang and Howard**—NOAA/OAR/National Severe Storms Laboratory, Norman, Oklahoma; **L. Tang, Langston, and Kaney**—Cooperative Institute for Mesoscale Meteorological Studies, University of Oklahoma, Norman, Oklahoma

Flash floods and river floods remain a top cause for weather-related disasters in Asia (IFRC 2018), causing large losses in commerce and human lives each year. Flood and mudslide warnings and predictions in Taiwan are especially challenging because of the complex and steep terrain and extreme rainfall produced by typhoons and quasi-stationary fronts. Advancements in weather radar and computer technologies in recent decades have provided meteorologists and hydrologists new opportunities to improve the monitoring and prediction of flash floods and debris flows (e.g., Germann et al. 2006; Tabary 2007; Zhang et al. 2011, 2016; Gourley et al. 2017). Over the last two decades, Taiwan Central Weather Bureau (CWB) in collaboration with the Water Resources Agency (WRA) has deployed a network of weather radars encompassing Taiwan and adjacent ocean (Fig. 1). The Soil and Water Conservation Bureau (SWCB) joined the collaboration since 2005 and the Construction and Planning Agency (CPA) joined in 2019. All four agencies now support the maintenance of the radar network and the research and development of radar applications for meteorological and hydrological predictions in Taiwan.

The annual rainfall in Taiwan is abundant and varies from 1,600 to 3,100 mm with an average of approximately 2,400 mm (Kuo et al. 2016). Further, very heavy rainfalls can occur in the warm season (May–October) with a maximum rate of more than 100 mm h^{-1} (e.g., Ching et al. 2011; Jou et al. 2016). To minimize the potential attenuation from the heavy rainfalls, the Taiwan weather radar network started with four S-band Doppler single-polarization radars (RCWF, RCCG, RCKT, and RCHL; Fig. 1), which were deployed between 1996 and 2002. One of them (RCWF) was upgraded to dual polarization in 2014. Each S-band radar has a maximum of ~460-km coverage and the initial network provided 24/7 surveillance for the Taiwan Island and surrounding ocean areas, revealing detailed rainfall and circulation structure of severe storms, typhoons, and mei-yu. For an island that is only ~150 km wide (east–west) and 400 km long (north–south), the network seemed to be more than sufficient in terms of the horizontal coverage. However, due to the two major mountain ranges [i.e., the Snow Mountain Range (SMR) and Central Mountain Range (CMR); Fig. 1] in the middle of the island and the severe blockages introduced, the vertical coverage of the S-band radar network in the inner island was severely limited. Large areas along the SMR and CMR have no radar coverage for the lowest 1 km of the atmosphere (Fig. 2a). This vertical coverage deficiency significantly limited the quality of the precipitation forcing for hydrological predictions and additional radars are necessary to mitigate such deficiencies. Given the size of the island and the complex terrain, additional long-range S-band radars did not seem to provide the best cost–benefit outcome. X-band radars, on the other hand, are subject to severe attenuation in the heavy rainfall of Taiwan environment and are insufficient to compensate all the gaps in the S-band network. Therefore, C-band radars seemed to provide an optimal supplemental network given its generally lower cost than S band and much better range coverage than X band. X-band radars, with the most flexibility of implementation among the three bands, are still being considered for a further compensation of small gaps in the S- and C-band radar network. Such gaps include areas of small basins in the complex terrain where low-level radar observations are important for flash floods and mudslides warnings.

The first three C-band dual-polarization (C-pol) radars (RCCK, RCMK, and RCGI; Fig. 1) being integrated into the CWB weather radar network were from the Taiwan Air Force, two of them

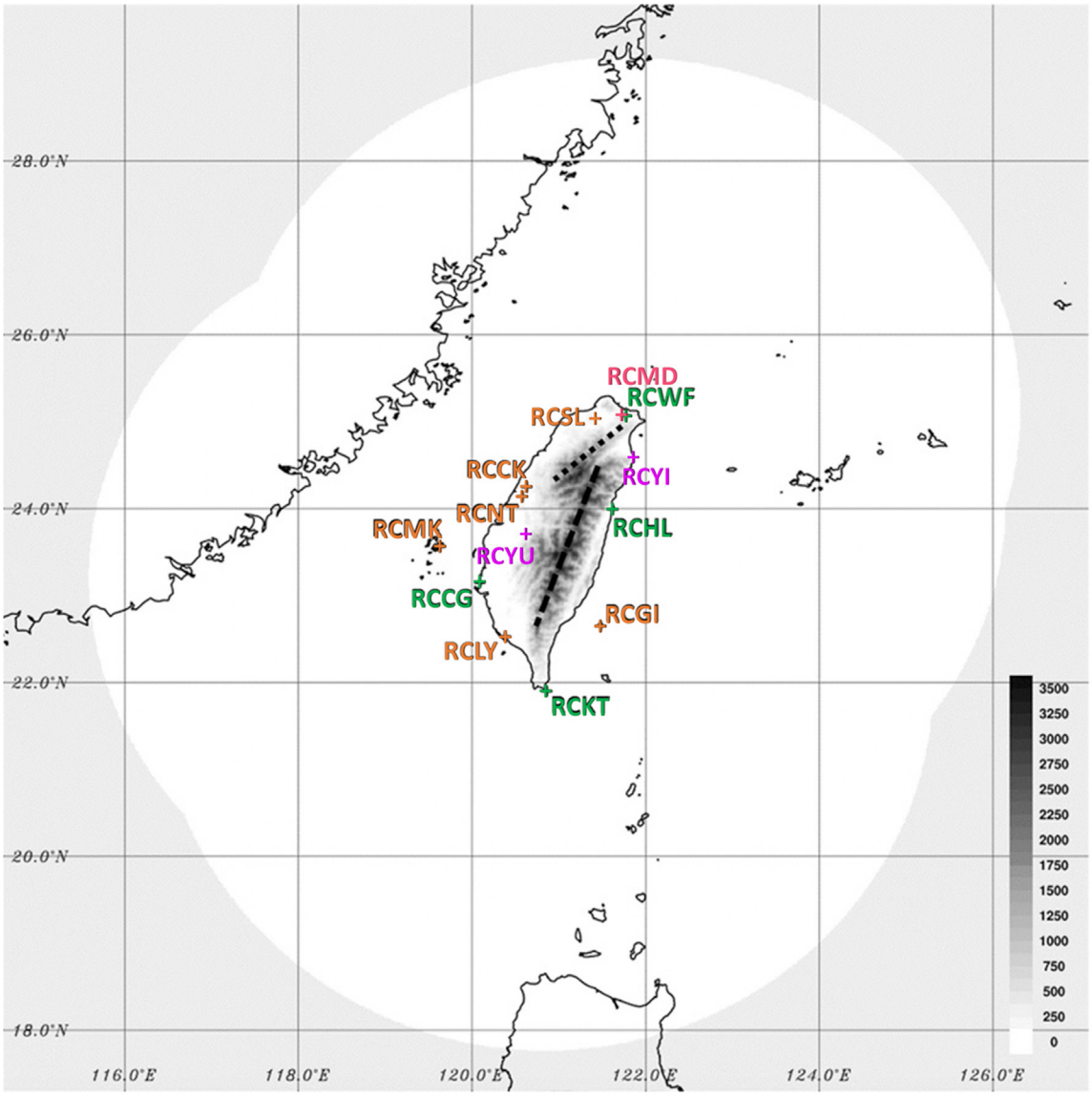

Fig. 1. The weather radar network in Taiwan. Green and orange plus symbols and four-letter identifiers (IDs) indicate the operational S- and C-band radars, respectively. RCYU and RCYI are C-pol radars that have not been deployed as of July 2020 and RCMD is a special C-pol radar collocated with RCWF for the calibration, training, and scan strategy design of the C-pol radars. The white region shows the maximum range of the radar coverage and gray shades the ground elevation. The black dotted line indicates the Snow Mountain Range and the dashed line the Central Mountain Range.

(RCCK and RCMK) in 2009 and one (RCGI) in 2016. Since 2016, four additional C-pol radars (RCMD, RCLY, RCNT, RCSL; Fig. 1) have been deployed island-wide to further improve the low-level radar coverage, among which the RCMD is a special radar collocated with RCWF for the calibration, training, and scan strategy design of the C-pol radars. Two more C-pol radars (RCYU, RCYI; Fig. 1) will be deployed in the next 3 years. The C-pol radars added significantly better low-level coverage, especially along the east coast and in large areas of northwestern and southern Taiwan (Fig. 2b).

The current operational network (Table 1) consists of one S-band dual-polarization (RCWF), three S-band single-polarization (RCHL, RCCG, and RCKT) and six C-pol (RCCK, RCMK, RCGI, RCLY, RCNT, and RCSL) radars. All radars were manufactured by LEONARDO Germany GmbH except for RCWF, which was made by Raytheon and Unisys. And all radars are maintained by CWB except for RCCK, RCMK, and RCGI, which are maintained by the Taiwan Air Force.

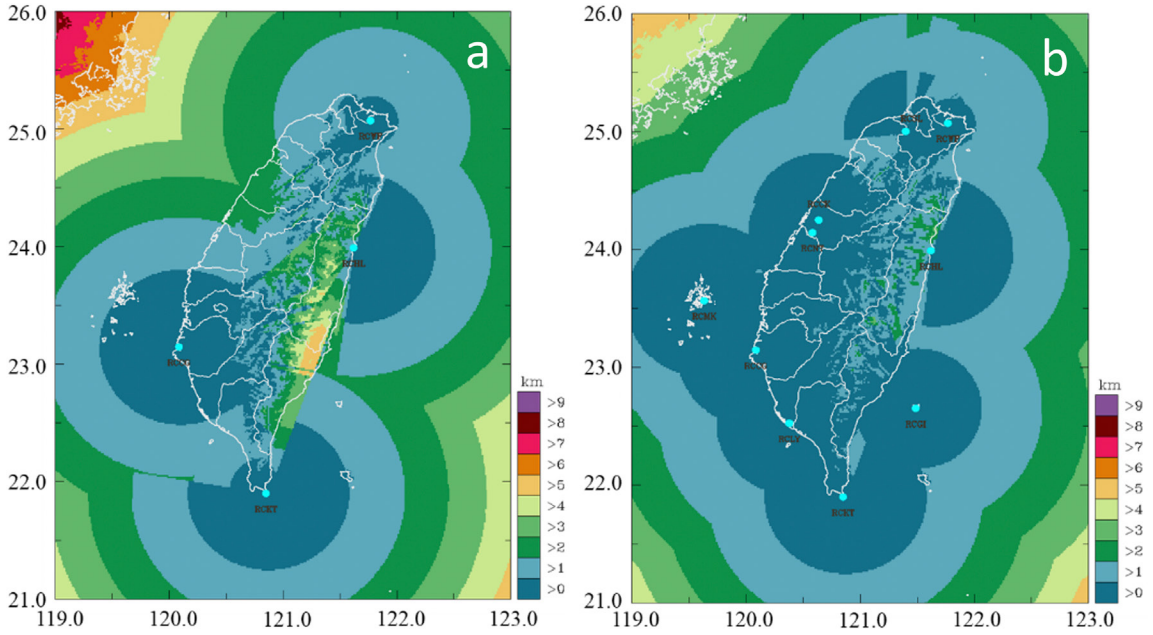

Fig. 2. Mosaicked heights of the lowest radar bins with ≤50% blockages from (a) the operational S-band and (b) the operational S- and C-band radar network.

CWB carries out preventive maintenance on the radar network (except for the Air Force radars) regularly. Further, the manufacturer technicians perform annual maintenance and calibrations on each radar to ensure the accuracy of the radar measurements.

Taiwan has deployed a dense rain gauge network consisting of 1,000+ radio telemetered sites (Fig. 3). This dense gauge network with an average spacing of ~6 km is managed and maintained by several government agencies including the CWB, WRA, SWCB, and Taipei City government. The tipping-bucket gauges report 10-min accumulations every 10 min. The stations are closely monitored by human and the data are quality controlled with automated algorithms as well as manually.

As the radar and surface observational network expanded, a system was required to seamlessly integrate the observational networks into a single platform. To address this need, the CWB and the National Severe Storms Laboratory (NSSL) of the U.S. National Oceanic and Atmospheric Administration (NOAA) established a joint scientific research collaboration in 2002. The collaboration resulted in the development and operational deployment of the Quantitative Precipitation Estimation and Segregation Using Multiple Sensors (QPESUMS) system. The basic infrastructure of the Taiwan QPESUMS system was based on an early version of the Multi-Radar Multi-Sensor (MRMS; Zhang et al. 2016) system developed by NSSL. However,

Table 1. Technical specifics of the Taiwan operational weather radar network.

Radar ID	Wavelength and polarimetry	Model	Sensitivity Z_{min} at 50 km (dBZ)	Power (KW)	Beamwidth (°)
RCWF	S dual	WSR-88D	–23.0	700	0.925
RCHL, RCCG, RCKT	S single	Meteor 1500S	~–20.0	750	~1.0
RCCK	C dual	Meteor 1600C	–10.5	250	0.95
RCMK	C dual	Meteor 1600C	–13.5	250	0.93
RCGI	C dual	Meteor 1700C	–13.7	250	0.895
RCLY	C dual	Meteor 1700C	–16.8	250	0.875
RCNT	C dual	Meteor 1700C	–12.7	250	0.901
RCSL	C dual	Meteor 1700C	–13.0	250	0.901

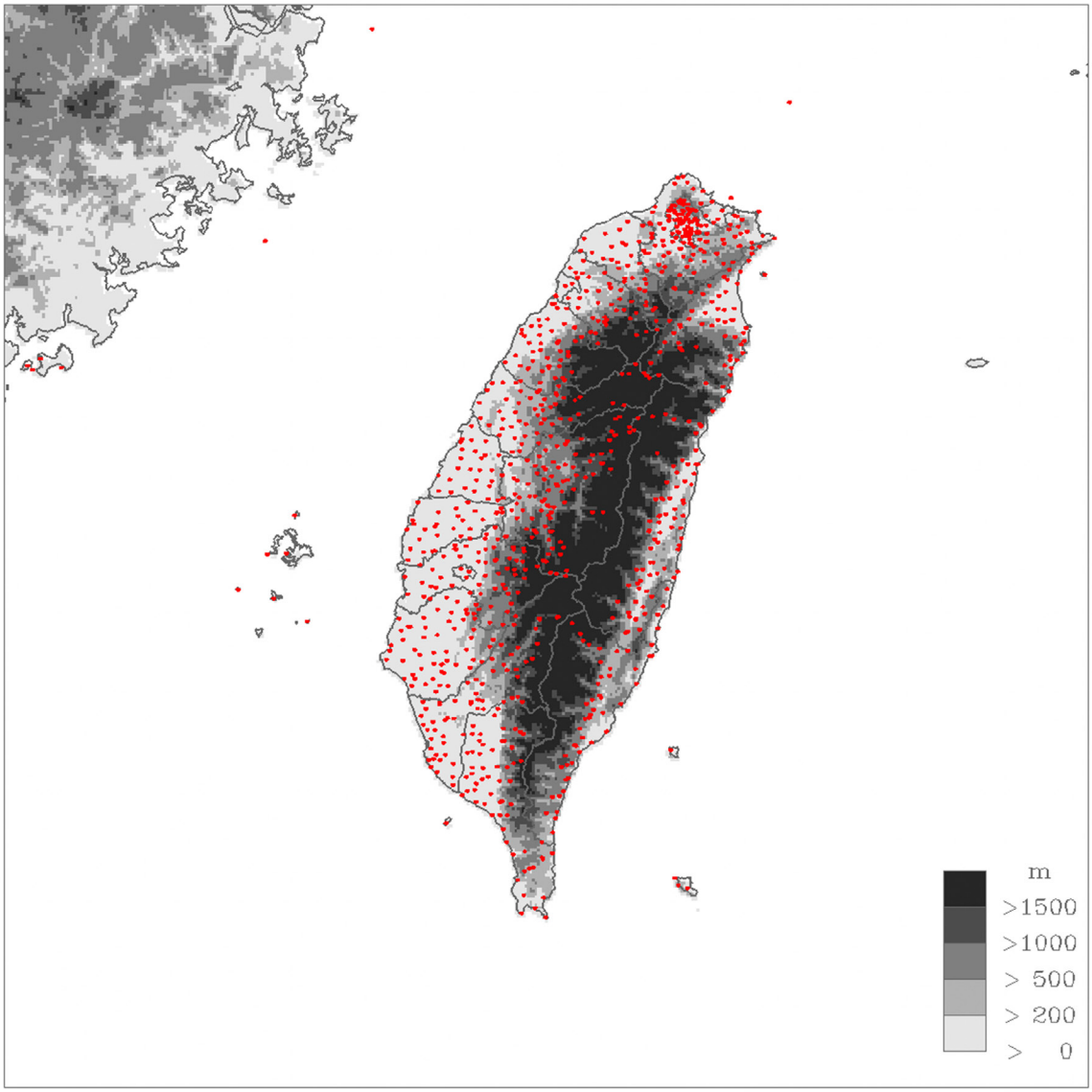

Fig. 3. Taiwan rain gauge network. Red dots represent over 1,000 gauge sites deployed and managed by Taiwan Central Weather Bureau, Water Resources Agency, Soil and Water Conservation Bureau, and Taipei City government.

Taiwan's geographical and climatological environment and its radar network composition are unique and different than the United States. Therefore the workflows within the QPESUMS are customized for the local data networks and the various algorithms [e.g., radar data quality control (QC), quantitative precipitation estimation (QPE)] are tuned according to the local environment. The QPESUMS system went into operations at CWB in 2004 and has evolved with new radars and advanced radar applications since then.

The QPESUMS system integrates multiple mixed band radars, gauges, and numerical weather prediction (NWP) model analysis data to generates a suite of high-resolution (1 km, 10 min) QPE and severe weather products that support CWB operations and many other government agencies. The 3D reflectivity mosaic and QPEs generated by the system are used in high-resolution radar data assimilation and for the verification of NWP model forecasts (e.g., Chen et al. 2020; Liu et al. 2020; Sun et al. 2020). The system also facilitates collaborations with academic communities for research and development of radar applications including QPE and nowcasting. This paper provides an overview of the operational QPE capabilities in the Taiwan QPESUMS system.

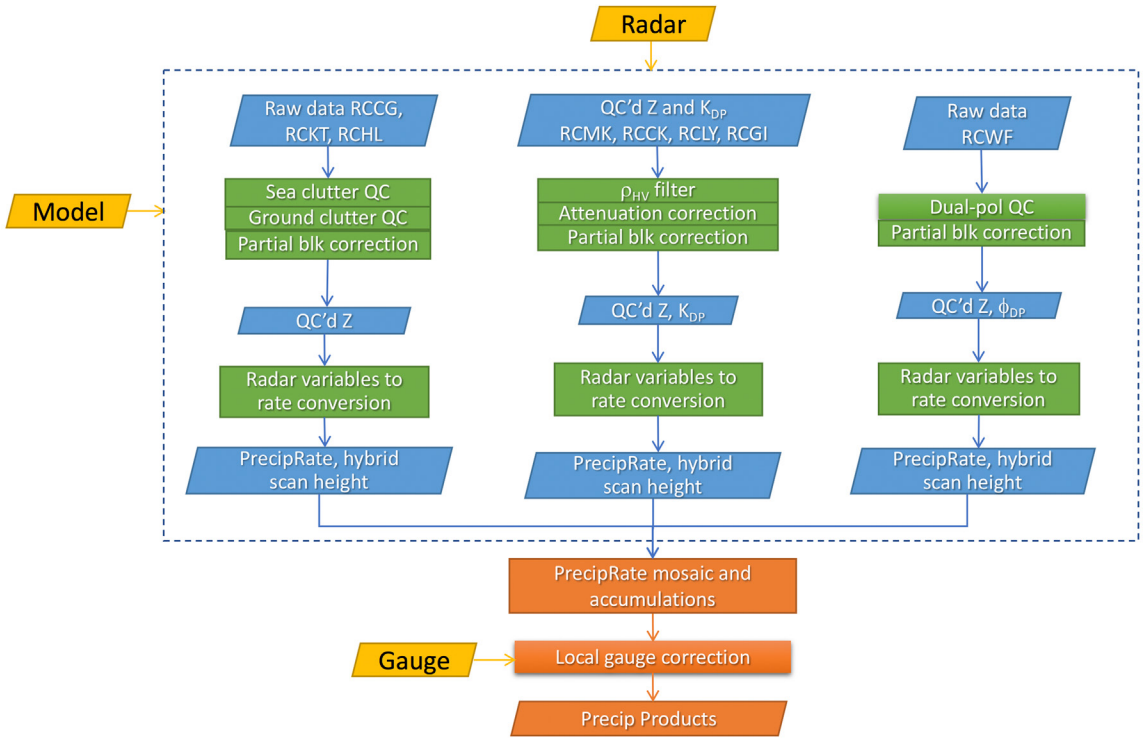

Fig. 4. An overview flowchart of the Taiwan QPESUMS system.

System overview

An overview flowchart of the Taiwan operational QPESUMS system is shown in Fig. 4. Three groups of single-radar modules (green rectangles, Fig. 4) were developed to process the S-band single-pol, C-band dual-pol, and S-band dual-pol radars, respectively. The single-radar processes generate quality controlled radar moments including reflectivity Z, differential reflectivity Z_{DR}, correlation coefficient ρ_{HV}, and differential phase ϕ_{DP} and a 2D precipitation rate field for each volume scan. The precipitation rate fields are then mosaicked onto a Cartesian grid and a number of accumulation products (1–72 h) are generated. A full list of QPE products is shown in Table 2 and brief descriptions of the functions in the single-radar and mosaic modules are provided below.

Single-radar quality control. The complex ocean and land geography in Taiwan posed many challenges in the radar data QC. Weather radar is designed to measure the concentration, size, and shape of hydrometeors, but it inevitably detects nonhydrometeor targets in the air such as insects and birds. Further, the radar beam may "anomalously" propagate (AP) through atmosphere such that its path bends lower than what would be expected under a standard atmosphere, hits the Earth surface, canopy, and manmade structure such as telecommunication

Table 2. List of key QPE products from the Taiwan QPESUMS system.

Product ID	Unit	Frequency	Product description
inst_rate_rad	mm h^{-1}	10 min	Instantaneous precipitation rate from radar QPE
rain01h_rad, rain03h_rad, …, rain72h_rad	mm	10 min	1 (3, 6, 12, 24, 48, 72)-hourly radar QPE accumulations
rain01h_gage, rain03h_gage, …, rain72h_gage	mm	10 min	1 (3, 6, 12, 24, 48, 72)-hourly gauge QPE accumulations
cb_rain01h_rad_gc, cb_rain03h_rad_gc, …, cb_rain72h_rad_gc	mm	10 min	1 (3, 6, 12, 24, 48, 72)-hourly local gauge bias-corrected radar QPE accumulations

towers, wind farms, ocean ships, and wave crests (sea clutter). These nonhydrometeor echoes are considered "clutter" in weather radar observations. While clutter mitigations were provided by the radar manufacturers during the signal processing (Table 3), considerable efforts were expended to develop a series of radar QC applications within the QPESUMS system to address

Table 3. Clutter mitigation in the signal processor/level-1 data for Taiwan radars.

Radar ID	Clutter filter in signal processor	Selected references
RCWF	Clutter mitigation decision (CMD), Gaussian model adaptive processing (GMAP)	Meymaris et al. (2015), Nguyen and Chandrasekar (2013), Siggia and Passarelli (2004), Tang et al. (2012)
RCHL, RCCG, RCKT	Fast Fourier transform (FFT)	
RCCK, RCMK, RCGI, RCLY, RCNT, RCSL	Infinite impusle response filter (IIR), discrete Fourier transform (DFT), generalized inner product	

residual data quality issues for the mixed radar wavelengths, single versus dual polarization, and the characteristics of the individual radar sittings. The main objective of all the single-radar QC modules (Fig. 4) is to identify such clutter from radar observations and to minimize their contamination in the precipitation products.

The S-band single-pol QC module involves three steps: 1) range profile clutter removal, 2) ground clutter filter, and 3) blockage compensation. The range profile clutter removal was based on a technique shown in Lakshmanan et al. (2010) for the identification of "bloom" echoes associated with birds and insects. Most of the bloom, sea clutter, and clear air echoes have a unique distribution of reflectivity that is relatively uniform across azimuth. Along the radial direction, the reflectivity tends to monotonically decrease with range up to some distance from the radar. The distance is associated with the maximum height to which the biological, boundary layer air disturbances, and sea clutter echoes can reach. Based on the reflectivity intensity and the slant range profile of reflectivity, the majority of such clutter was removed, especially when they were not connected to precipitation echoes. Ground clutter was mitigated via two steps. Persistent clutter from mountain peaks was filtered by subtracting a static clutter map derived from long-term reflectivity statistics (P.-L. Chang et al. 2009). A neural network-based QC (Lakshmanan et al. 2007) was then applied to further mitigate residual and transient ground clutter. Figure 5 shows example reflectivity fields from RCCG before and after the S-band single-pol QC. The 0.5°-tilt raw reflectivity field (Fig. 5a) depicted the typhoon rainbands very well to the west but had severe blockage to the east. Close to the radar, there were light sea clutter/clear air echoes to the northwest (Fig. 5a) and ground clutter to the east. The ground clutter was confirmed by human expert by examining a time series of reflectivity fields and the vertical cross sections. The range profile clutter QC (Fig. 5b)

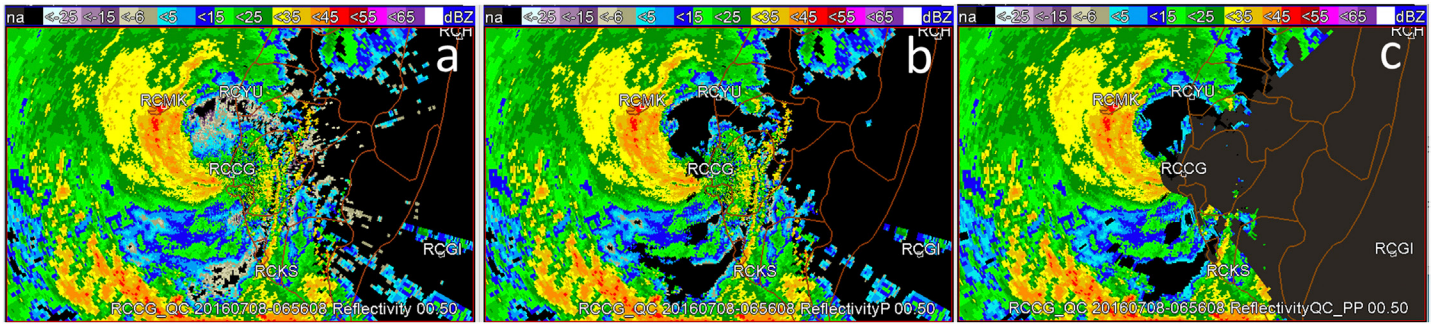

Fig. 5. Base reflectivity (a) before QC, (b) after sea clutter QC, and (c) after the ground clutter QC. The data were from RCCG valid at 0656 UTC 8 Jul 2016.

removed the light sea clutter/clear-air echoes and the climatology based and neural network QC (Fig. 5c) removed the ground clutter to the east of the radar.

After the QC, a blockage correction was applied to the reflectivity field as follows:

$$Z_{\text{corr}} = Z_{\text{obs}}/(1 - \beta), \tag{1}$$

where Z_{obs} is the observed reflectivity factor ($\text{mm}^6\ \text{m}^{-3}$) and β is a ratio of the two-way power loss due to beam blockage over the total power in a given radar bin.

The S-band dual-pol QC is a physically based scheme developed by Tang et al. (2014), in which a simple filter based on correlation coefficient (ρ_{HV}) was applied to create a first-guess separation of hydrometeor ($\rho_{\text{HV}} > 0.95$) and nonhydrometeor ($\rho_{\text{HV}} \le 0.95$) echoes. Several steps were then taken to handle hydrometeors (e.g., melting snow aggregates, hail) with low ρ_{HV} (≤0.95) and nonhydrometeors (e.g., very weak clear air echoes) with high ρ_{HV} (>0.95). Specifically, the freezing-level height was combined with radar data to delineate the melting layer (ML) in radar observations and a relaxed ρ_{HV} criteria (≤0.70) was applied to screen nonhydrometeor echoes in the ML. The freezing-level height was obtained from the Space and Time Multiscale Analysis System (STMAS; Xie et al. 2011) analysis data. Hail is usually associated with deep convections and tall clouds. Thus, echo tops and reflectivity intensities were used to delineate potential hail areas and then a lower ρ_{HV} threshold was used to identify nonhydrometeors. Very weak echoes with abnormally high ρ_{HV} values were checked on their horizontal and vertical continuities. If these echoes were very small in size and not connected to a significant area of hydrometeors, they are classified as clear air echoes. Figure 6 shows examples of reflectivity fields before (Fig. 6a) and after the S-band dual-pol QC (Fig. 6b). Due to the additional variables of ρ_{HV} (Fig. 6c) and differential reflectivity Z_{DR} (Fig. 6d), the dual-pol QC was able to identify echoes associated with biological (e.g., birds and butterflies) and other nonhydrometeor targets in the Shitou Shan mountain region (white curves, Fig. 6). The echoes to the northwest of the white curve were associated with a mix of high and low ρ_{HV} values. An examination of the gauge data (not shown) indicated scattered rain in the area. The dual-pol QC tried to preserve the spatial integrity of the rain echoes and thus retained some nonhydrometeor pixels connected to the rain. It did remove those nonhydrometeor pixels with spatially consistent low ρ_{HV} values (i.e., the holes to the north of the white curve, Fig. 6b).

The C-band dual-pol radar QC includes a simple filter that removes data associated with a low ρ_{HV} value (default threshold = 0.80). The simple filter appears to be sufficient since the C-band dual-pol radar manufacturer provides quality-controlled fields (Table 3) and the ρ_{HV} filter is applied on the quality-controlled data. In addition, an attenuation correction was applied to the Z field given the fact that shorter wavelength radars are subject to more significant attenuation than longer wavelengths. The attenuation correction was based on a method proposed by Bringi et al. (1990), in which the adjustment to reflectivity is calculated by

$$Z_{\text{adj}}(r) = Z_{\text{obs}}(r) + \alpha \times [\phi_{\text{DP}}(r) - \phi_{\text{DP}}(0)], \tag{2}$$

where r is the range and the factor $\alpha = 0.08$ dB per degree was estimated from the Taiwan local disdrometer data (Wang et al. 2016, hereafter W16). This linear method was chosen for its simplicity and computational efficiency. However, it is not constrained like some of the more sophisticated techniques [e.g., the ZPHI method by Testud et al. (2000)] and can be unstable with a noisy ϕ_{DP} field. To minimize the instability, the ϕ_{DP} field was preprocessed for unwrapping and range smoothing to minimize the noises in the field (W16) and a sanity check was applied to avoid any negative corrections.

Figure 7 shows examples of reflectivity fields before and after the attenuation correction. Before the correction (Fig. 7a), RCMD (C band) radar base reflectivity was significantly lower

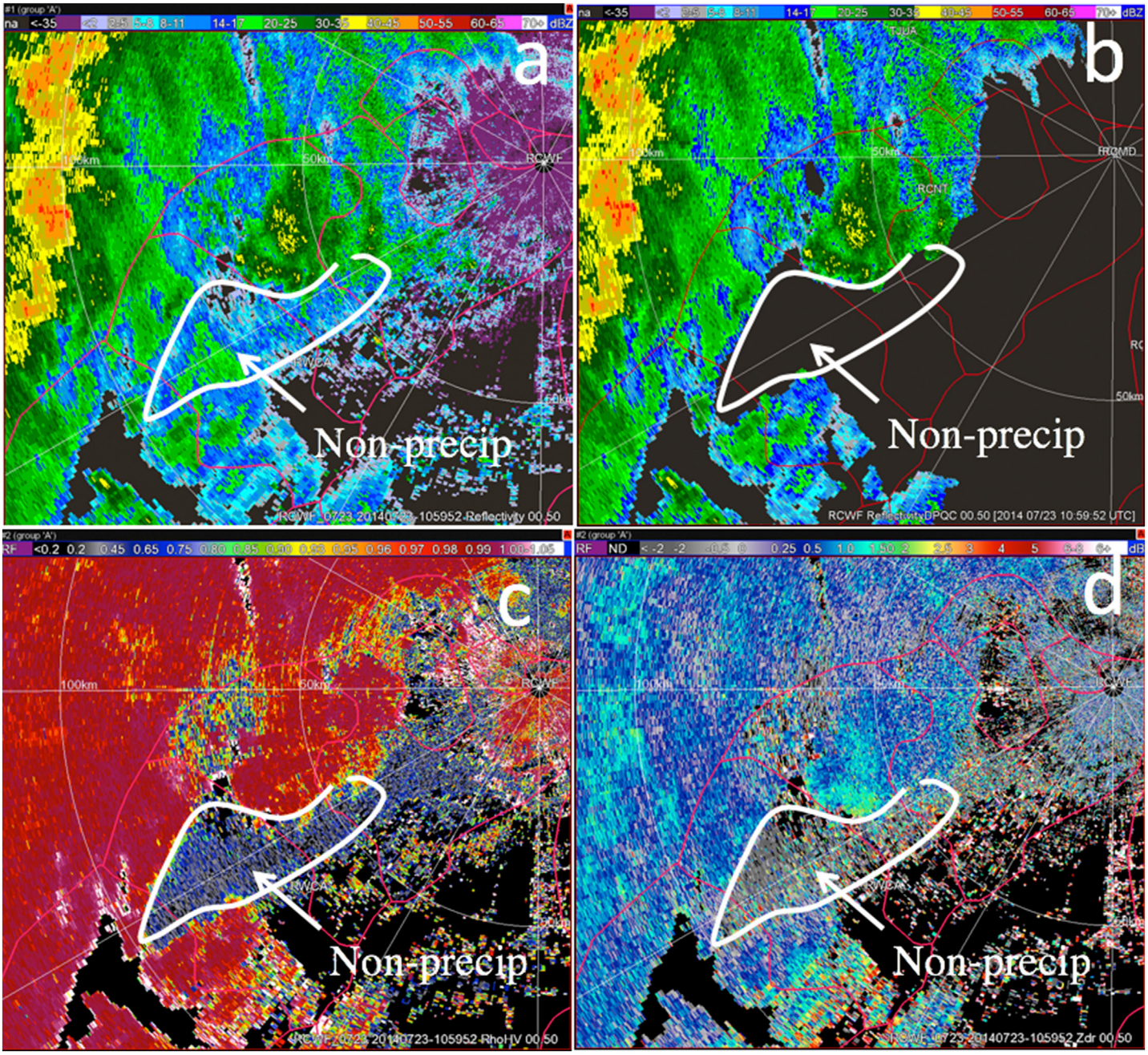

Fig. 6. Base reflectivity fields (a) before and (b) after dual-pol QC and the dual-pol (c) ρ_{HV} and (d) Z_{DR} fields. The data were from RCWF at 1100 UTC 23 Jul 2014. The white curve indicates an area of nonhydrometeor echoes.

than the base reflectivity of the same area from RCWF (S band, Fig. 7c), especially beyond 50 km north of RCMD (blue circle, Fig. 7a). The severe attenuation of reflectivity was due to a heavy rainfall near the radar (Fig. 7a). After the correction, reflectivity field from RCMD (Fig. 7b) agreed better with the S-band observations (Fig. 7c). Figures 7d and 7e show the difference between the RCWF and RCMD reflectivities as a function of the distance from RCWF. Before the correction, the differences were centered at ~5 dB*Z* (white dashed line, Fig. 7d). After the correction the center of the differences were brought down to ~0 dB*Z* for all the distances (white dashed line, Fig. 7e) except for beyond 220 km where RCWF reflectivities appeared to be lower than those from RCMD. The higher RCMD reflectivities at these far ranges might be due to the small bias of attenuation correction accumulated over a long path. The correction also significantly reduced the spread of the RCWF–RCMD reflectivity differences (Fig. 7d vs Fig. 7e).

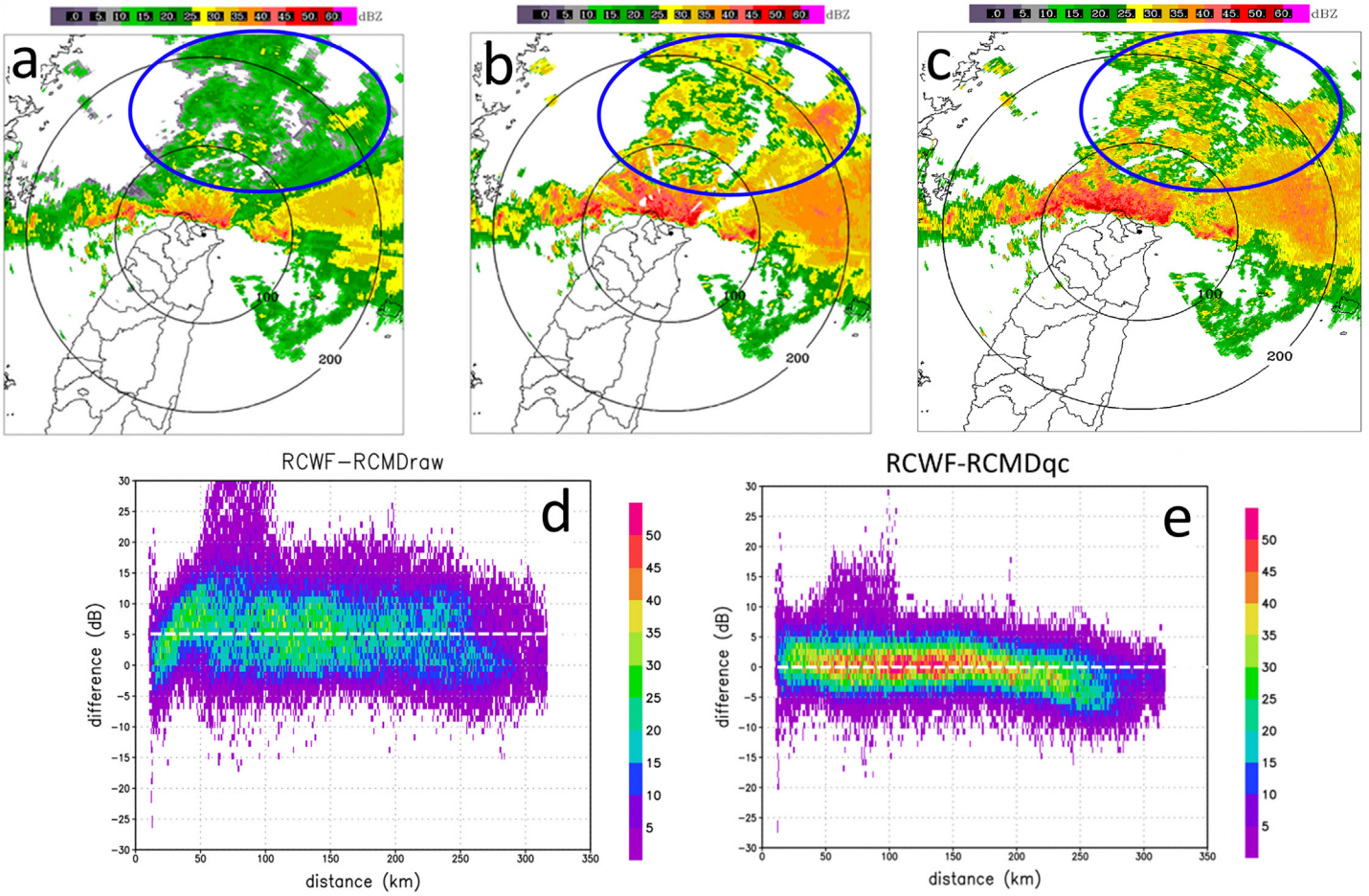

Fig. 7. Base reflectivity field at 0018 UTC 2 Jun 2017 from RCMD radar (a) before and (b) after the attenuation correction. (c) The base reflectivity from RCWF at the same time. The reflectivity differences (RCWF – RCMD) (d) before and (e) after the attenuation correction are also shown. The black circles in (a)–(c) are 100- and 200-km range rings, respectively, and blue circle indicates an area of severe attenuation in RCMD.

The current attenuation correction only accounts for attenuation in the path of radar beams but not the wet radome effect. The wet radome effect is related to the rain or snow water coating the radar radome and causing attenuation in Z and errors in Z_{DR}. The CWB in collaboration with the Taiwan National Central University (NCU) is evaluating the wet radome issues in C-pol radar data and a correction based on the self-consistency method by Vivekanandan et al. (2003) is under development.

Single-radar precipitation rate estimation. A key objective in the CWB–NSSL collaboration was developing a high-resolution and high-accuracy QPE for the Taiwan environment. As with data QC, there was a significant effort to understand the precipitation characteristics and then develop a series of QPE methodologies that could be refined over time for each radar system. Precipitation rate fields are derived from individual radars via different methodologies depending on the radar types (Fig. 4). A brief description of each method is as follows.

S-BAND SINGLE-POL. Precipitation rate estimates for the S-band single-pol radars (RCCG, RCKT, and RCHL) are calculated from the seamless hybrid scan reflectivity (SHSR; Zhang et al. 2016). SHSR is a 2D field consisting of the lowest (altitude) radar reflectivity observations that do not have significant blockages (i.e., two-way power loss ≤ 60%, an adaptable parameter) and partially (0%–60%) blocked reflectivity data were corrected according to Eq. (1). Figure 8 shows blockage and base reflectivity fields from 0.5°, 1.45°, and 2.4° tilts and the associated SHSR field from RCCG around 1745 UTC 15 August 2019. The RCCG radar is severely blocked by

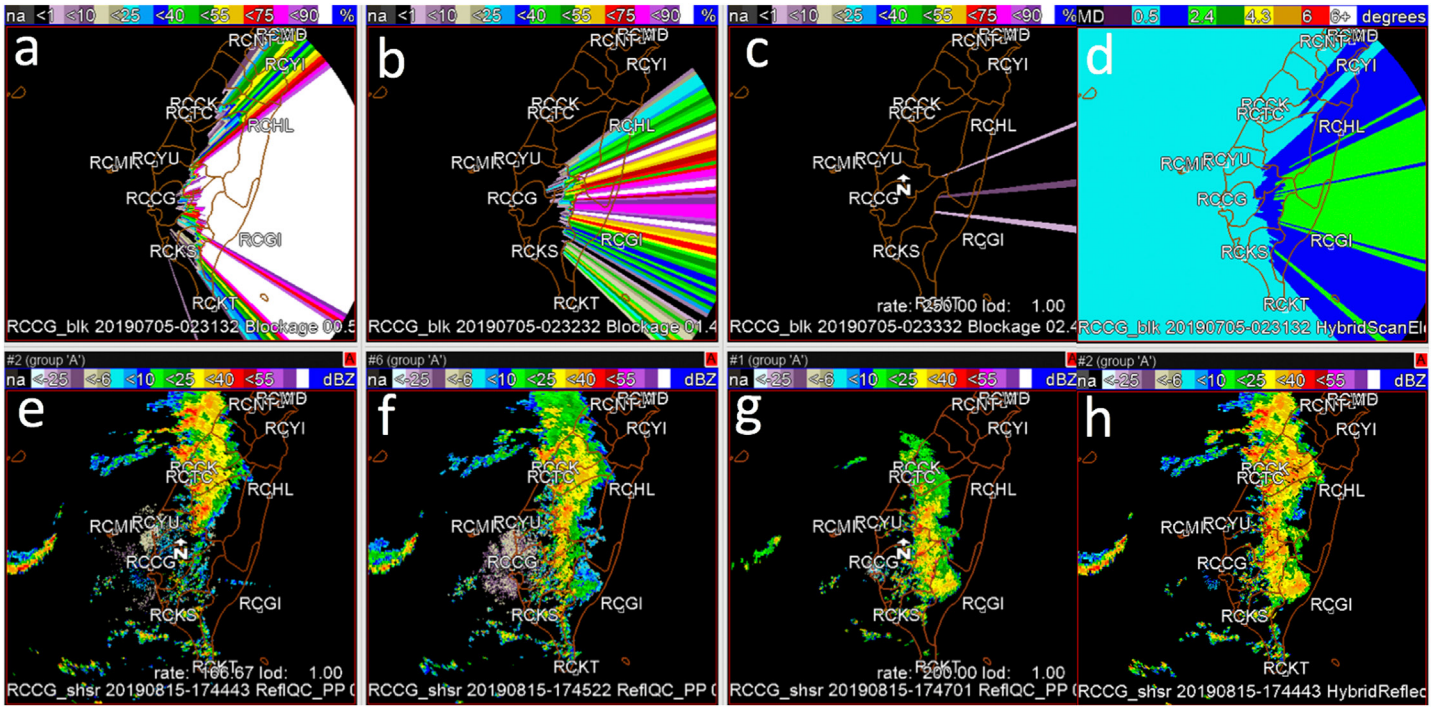

Fig. 8. (a)–(c) Blockage and (e)–(g) base reflectivity fields from RCCG at (a),(e) 0.5°, (b),(f) 1.45°, and (c),(g) 2.4° tilts. (d) The hybrid scan tilts and (h) the seamless hybrid scan reflectivity are also shown. The data were valid at ~1745 UTC 15 Aug 2019.

the CMR to the east, especially in the lowest two tilts (Figs. 8a–c). Therefore, the hybrid scan (Fig. 8d) consisted of data from the first tilt to the west and second and third tilt to the east. The SHSR field (Fig. 8h) combining the data from 0.5°, 1.45°, and 2.4° tilts showed a better depiction of the precipitation system than each of the individual tilts (Figs. 8e–g).

The S-band single-pol radar SHSR field is converted into rain rate using an $R(Z)$ relationship. In the early years of QPESUMS when high-quality local drop size distribution (DSD) data in Taiwan was not readily available, the CWB meteorologists tested a number of $R(Z)$ relationships for typhoon events and found that the Xin et al. (1997, hereafter X97) $R(Z)$ relationship [Eq. (3)] consistently yielded better QPE results than other relations when compared with gauges:

$$Z = 32.5R^{1.65}. \tag{3}$$

Here R is the rain rate (mm h^{-1}). The better performance of Eq. (3) than the other relationships was due to the higher rain rates at low to moderate reflectivities (15–40 dBZ, Fig. 9), which better captured the high rainfall efficiency in typhoons where a large concentration of small drops (and liquid water content) was associated with modest reflectivities. Since QPESUMS was developed for operational flood monitoring and warnings in Taiwan, getting accurate estimates for heavy rain especially in typhoons was a priority and thus X97 was adopted for the S-band single-pol radar QPE.

Recent studies by Wang et al. (2012, hereafter W12) and W16 generated several local $R(Z)$ relationships (Fig. 9) using DSD data from four Joss–Waldvogel disdrometers (JWDs) in northern Taiwan during selected northeastern front, mei-yu, and typhoon events in 2011 and 2012. It is apparent that the X97 $R(Z)$ relationship is very close to the W12 typhoon $R(Z)$ relationship ($Z = 30.7R^{1.65}$, Fig. 9). The similarity of the two may explain why X97 yielded more accurate QPEs for heavy typhoon rainfalls than other empirical relationships in the early QPE experiments. However, it should not be interpreted as they represent the same DSDs, since the X97 was an empirical relationship derived from the gauge and C-band radar data in Edmonton, Canada where the radar reflectivities were not corrected for attenuation. The high rain rates

for low to moderate reflectivities in the X97 relationship were most likely a compensation effect for the attenuated reflectivities.

S-BAND DUAL-POL. Precipitation rates from S-band dual-pol radar (RCWF) are derived from a combination of specific attenuation (A), specific differential phase (K_{DP}), and reflectivity (Z). The scheme is similar to Wang et al. (2019) and is briefly reintroduced below for easy reference:

$$A(r) = \frac{[Z_a(r)]^b C(b,\mathrm{PIA})}{I(r_1,r_2) + C(b,\mathrm{PIA}) I(r,r_2)}, \tag{4}$$

where

$$I(r_1,r_2) = 0.46b \int_{r_1}^{r_2} [Z_a(s)]^b \, ds, \tag{5a}$$

$$I(r,r_2) = 0.46b \int_{r}^{r_2} [Z_a(s)]^b \, ds, \tag{5b}$$

$$\mathrm{C}(b,\mathrm{PIA}) = \exp(0.23b \times \mathrm{PIA}) - 1, \tag{5c}$$

$$\mathrm{PIA}(r_1,r_2) = \alpha \Delta\phi_{DP}; \text{ where } \Delta\phi_{DP} = \phi_{DP}(r_2) - \phi_{DP}(r_1). \tag{5d}$$

Here r is the range at a given gate, r_1 is the nearest gate with precipitation in a given radial, and r_2 the last precipitation gate or the gate just below the bottom of the ML, whichever is closer to the radar. The ML bottom was approximated by the mean of 10° and 0°C heights from the STMAS sounding at the radar site and $R(A)$ was applied in areas where the radar beam is completely below the ML bottom to avoid any ice contamination. Further, pixels in $[r_1, r_2]$

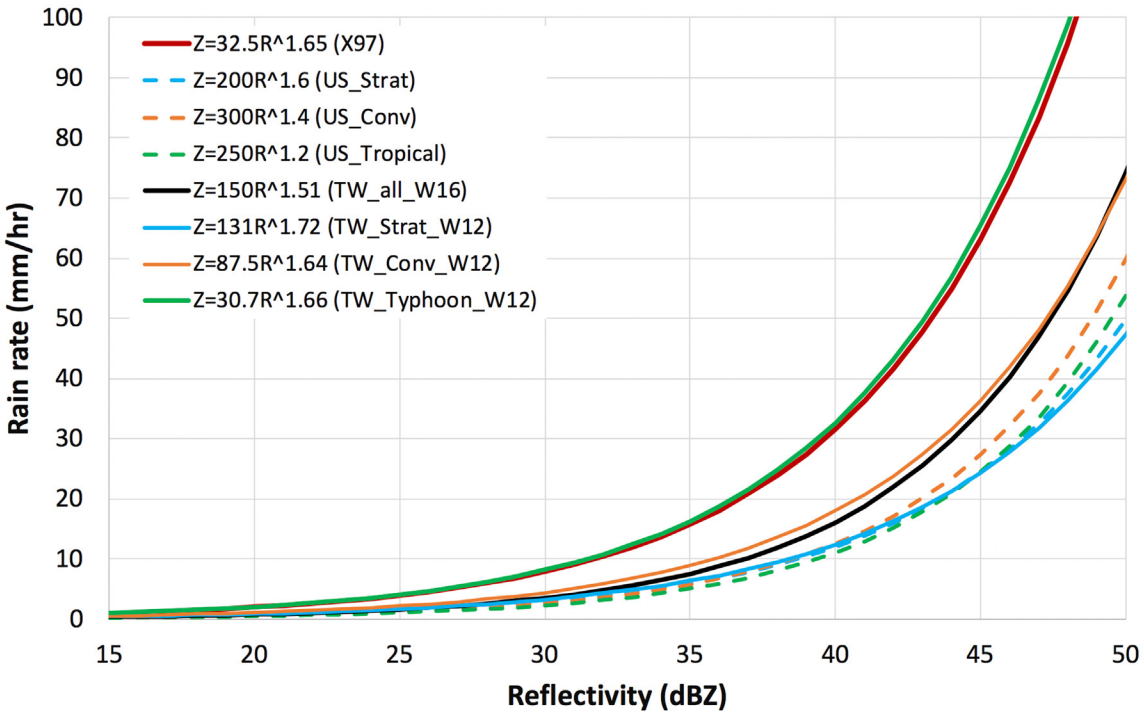

Fig. 9. $R(Z)$ relationships from X97, W12, W16, and the U.S. MRMS system.

with potential hail contamination are excluded from all the calculations. Parameter Z_a is the measured reflectivity, b is a constant (0.62 for S band; Ryzhkov et al. 2014), PIA is the path-integrated attenuation, and α is a parameter that generally varies with drop size distributions and with temperature (Ryzhkov et al. 2014). Note that reflectivity Z_a in Eq. (4) appeared in both the nominator and denominator, which effectively removes any systematic biases in the reflectivity observations when calculating A. Therefore, A is insensitive to systematic biases in Z_a such as those from partial blockage, calibration, and attenuation (Cocks et al. 2019; Zhang et al. 2020).

The precipitation rates are estimated from A where reflectivity is below 50 dBZ (an adaptable parameter):

$$R(A) = 4{,}120A^{1.03}. \tag{6}$$

Here the $R(A)$ relationship is for S band at 20°C (Ryzhkov et al. 2014) and A is calculated from Eqs. (4) and (5a)–(5d). While the $R(A)$ relationship is not sensitive to DSD variations (Ryzhkov et al. 2014), the attenuation is. The dependency is captured by reflectivity distributions [Eqs. (5a) and (5b)] and the parameter α [Eq. (5d)]. The parameter α is a function of the "Z_{DR} slope" K ($=dZ_{DR}/dZ$) (Wang et al. 2019; Zhang et al. 2020) and is calculated in real time for every volume scan to reflect DSD changes.

The 50 dBZ constraint is to prevent $R(A)$ from potential hail contamination. Above 50 dBZ, an $R(K_{DP})$ relationship is applied:

$$R = 47.5998\left|K_{DP}\right|^{0.7605}. \tag{7}$$

Equation (7) was derived using two-dimensional video disdrometer data obtained at NCU during July–September of 2000–07 (Chen et al. 2017).

Because the $R(A)$ method is applicable in rain areas only, the precipitation rate at ranges beyond the ML bottom was calculated from a combination of $R(Z)$, $R(Z, Z_{DR})$, and $R(K_{DP})$ relations as described in Giangrande and Ryzhkov (2008) based on a hydrometeor classification (Park et al. 2009). Figure 10 shows example base reflectivity, hydrometeor classification, and rain rate fields from RCWF ~2235 UTC 1 June 2017.

C-BAND DUAL-POL. The C-band dual-pol radar precipitation rate estimates are calculated from the following $R(K_{DP})$ and $R(Z)$ synthetic scheme:

$$R = 35.4\left|K_{DP}\right|^{0.799};\quad \text{if } R(K_{DP}) \geq 13 \text{ mm h}^{-1}, \tag{8}$$

$$Z = 150R^{1.51};\quad \text{if } R(K_{DP}) < 13 \text{ mm h}^{-1}. \tag{9}$$

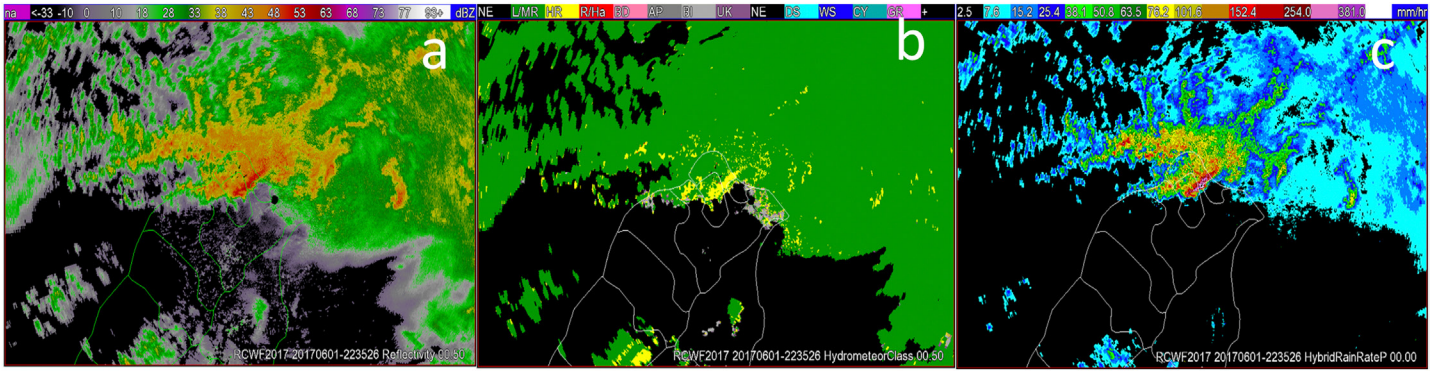

Fig. 10. Example-based (a) reflectivity, (b) hydrometeor classification, and (c) precipitation rate fields from RCWF at 2235 UTC 1 Jun 2017.

The $R(K_{DP})$ relationship was derived from 2D video disdrometer observations at NCU during 13 typhoon events from June 2001 to October 2005 (W.-Y. Chang et al. 2009; Wang et al. 2013, hereafter W13). A typhoon-based $R(K_{DP})$ relationship was applied for the higher amounts because other relationships tended to underestimate for the higher amounts. The $R(Z)$ relationship was based on ~7,920 min of DSD data from four JWDs in northern Taiwan. The data encompassed mei-yu and typhoon events in 2012 (W16).

Figures 11 and 12 show hourly QPE fields from two new C-pol radars, RCLY and RCNT, and a comparison with mosaicked single-pol S-band radar QPEs. The RCLY and RCNT QPE fields are generated using Eqs. (8) and (9) with 2-min update cycle using the three lowest elevations. In both cases, the C-pol QPE reduced the root-mean-square errors (RMSEs; Fig. 11c vs Fig. 11d and Fig. 12c vs Fig. 12d) and increased the correlation coefficients for

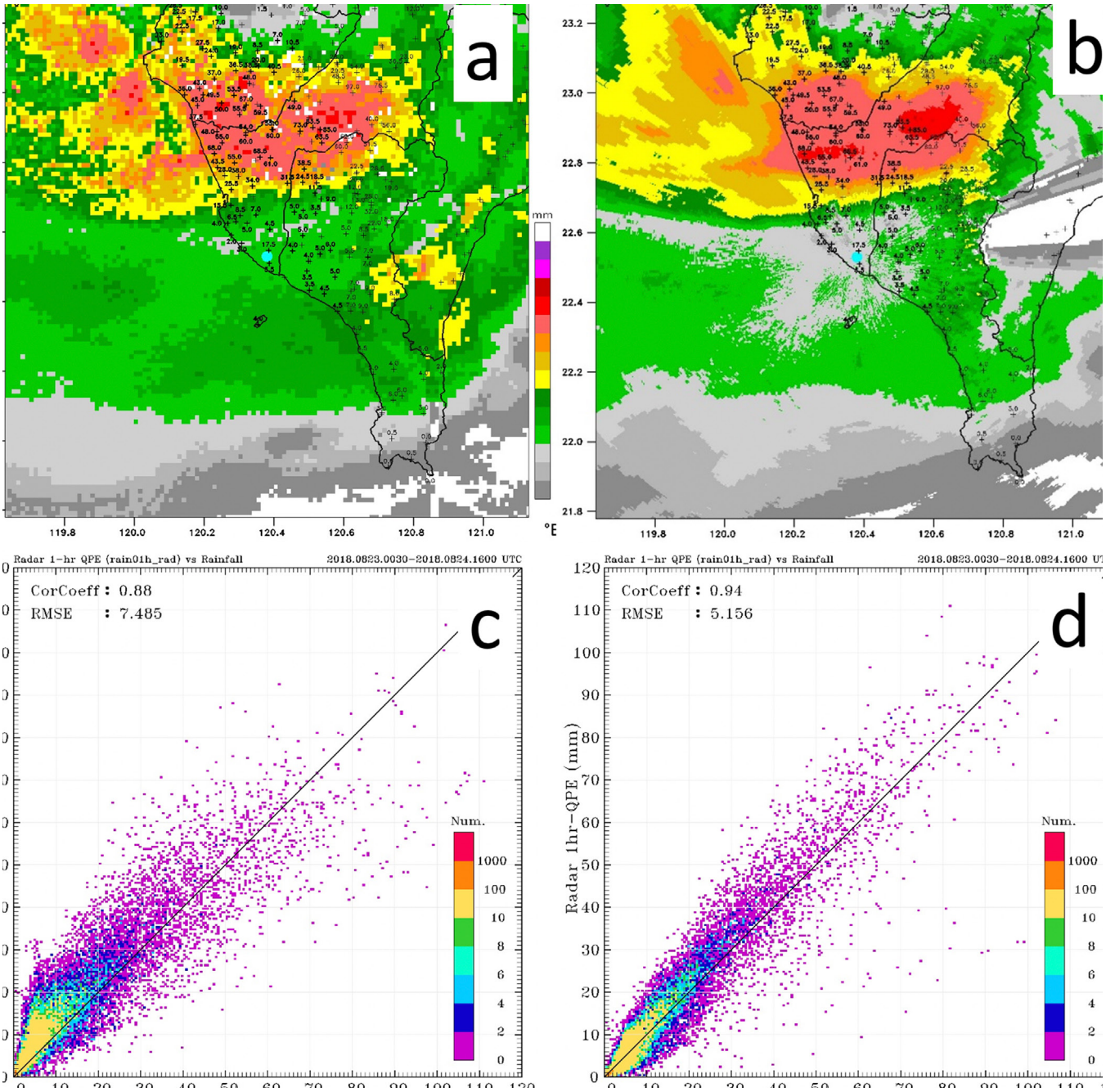

Fig. 11. Hourly (a) S-band single-pol radar QPE mosaic from RCCG and RCKT and (b) C-band dual-pol radar QPE from RCLY ending at 0500 UTC 23 Aug 2018. Scatterplots of the (c) S- and (d) C-band QPEs vs gauges were for 0030 UTC 23 Aug–1600 UTC 24 Aug 2018 and in areas with an elevation ≤ 500 m MSL.

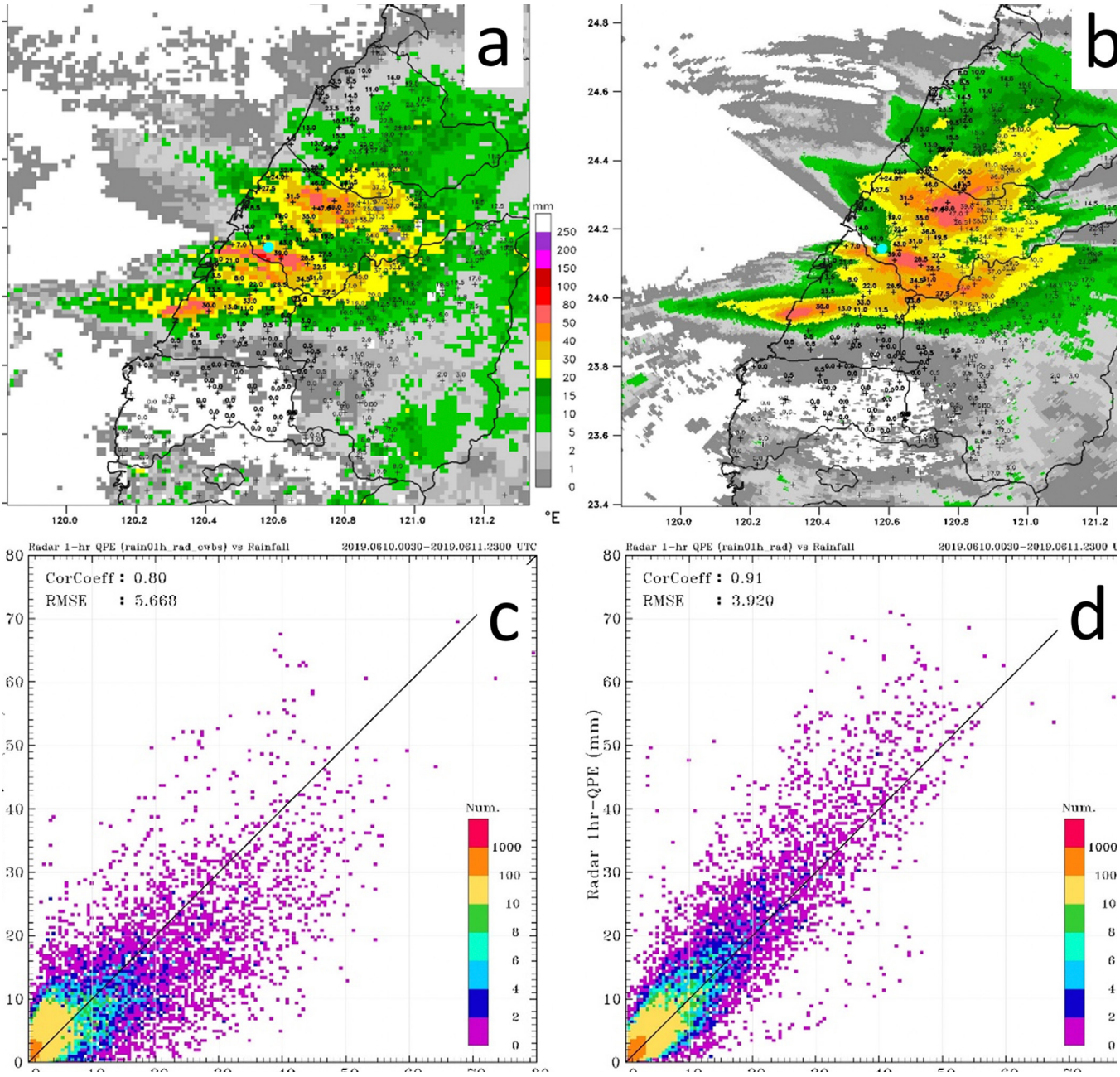

Fig. 12. As in Fig. 11, but for the mosaicked (a) S-band single-pol radar QPE and (b) C-pol radar QPE from RCNT ending at 0200 UTC 11 Jun 2019. Scatterplots of the (c) S- and (d) C-band QPEs vs gauges were for 0030 UTC 10 Jun–2300 UTC 11 Jun 2019 in areas with an elevation ≤ 500 m MSL.

areas with an elevation ≤ 500 m above mean sea level (MSL). In both events, the S-band single-pol QPE had a wet bias for the lighter amounts, but the bias was much prominent for the 23–24 August event (up to ~25 mm, Fig. 11c) and no so much for the 10–11 June 2019 event (only up to ~5 mm, Fig. 12c). There was even an underestimation bias for rainfall amounts above 10 mm (Fig. 12c) in the June 2019 event. The large variations of the biases in the S-band single-pol QPE showed the challenge of one $R(Z)$ not being able to capture the spatiotemporal variations of DSDs. On the other hand, a combination of the W16 general $R(Z)$ [Eq. (9)] and W13 typhoon $R(K_{DP})$ [Eq. (8)] in the C-pol QPE yielded a much improved QPE for light and heavy amounts for both events (Fig. 11d vs Fig. 11c and Fig. 12d vs Fig. 12c). The results demonstrated the advantage of dual-pol radar QPE relations [$R(Z)$ + $R(K_{DP})$] in better capturing the local DSDs than the single-pol radar $R(Z)$ relation. The improvements in the C-pol radar QPE were also attributed to 1) the locations of the C-pol radars provided

better low-level coverages than the S band in some of the precipitation areas (Fig. 2) and 2) the higher spatial (250 m) and temporal (2 min) resolutions of the C-pol radar data than the S-band (1 km, 10 min) data.

Precipitation rate mosaic and accumulations. The single-radar rain rate fields are mosaicked via a distance and height-weighted mean scheme, i.e.,

$$R_{\text{mosaic}} = \frac{\sum_{i=1}^{N} \text{wh}(h_i)\,\text{wd}(d_i)R_i}{\sum_{i=1}^{N} \text{wh}(h_i)\,\text{wd}(d_i)}, \tag{10}$$

where R_{mosaic} is the mosaicked rate and R_i the rate from an individual radar i; N is the total number of radars covering a given grid point; and wh and wd are the weights associated with the height and distance, respectively. The two weights are defined as

$$\text{wh}(h_i) = \exp(-h_i^2/H^2), \tag{11a}$$

$$\text{wd}(d_i) = \exp(-d_i^2/D^2), \tag{11b}$$

where d is the horizontal distance from the radar to the mosaic grid point and h the height of the radar data above the ground. Parameter H is a height scaling factor and has a default value of 2 km for all radars, and D is a distance scaling factor and has a default value of 50 km for single-pol radars and 150 km for dual-pol radars. The larger value of D for dual-pol radars allows more contributions from the dual-pol rate fields than their single-pol counterparts at the same distance given the better performance of the dual-pol QPE (e.g., W13; Ryzhkov et al. 2014; Cocks et al. 2019). Figure 13 shows an example mosaic rain rate field (Fig. 13a) and the single-radar rain rate fields from RCHL, RCCG, RCCK, RCKT, and RCMK (Figs. 13b–f, respectively) at ~0740 UTC 8 July 2016. It is clear that all of the single radars (except for RCMK) had significant blockages by the CMR in the middle of the Taiwan Island. The mosaicked rate was able to capture the typhoon system better than did any individual radars.

Based on the radar rain rate field, a number of radar QPE accumulations for different lengths are derived every 10 min (Table 2).

Local gauge-corrected radar QPE. The hourly radar QPE is adjusted based on gauge observations using a local gauge bias correction (LGC) scheme described in Zhang et al. (2008). The LGC calculates differences between hourly gauge observations and collocated radar estimates. The differences are then interpolated onto the QPESUMS Cartesian grid via an inverse-distance-squared weighting function. The radius of influence for the interpolation is 30 km, and the maximum number of gauges that impact a grid point is limited to 6. This constraint is imposed to avoid oversmoothing and to preserve gradients in the gauge observed precipitation distribution. The interpolated difference is then applied to the hourly radar QPE grid to obtain an LGC hourly QPE. The same interpolation scheme was also applied to gauge data to obtain an hourly gauge-only QPE (Table 2).

Figure 14 shows examples of the hourly radar-only QPE, gauge-only QPE, and LGC QPE. The radar-only QPE had significant overestimation in southeastern Taiwan (dashed white circle, Fig. 14a) when compared to the gauge-based QPE (Fig. 14b). Meanwhile, a narrow rainband in southwestern Taiwan (white circle, Fig. 14a) was much better defined in the radar QPE than in the gauge QPE. The difference showed the benefits of high-resolution radar observations in capturing small-scale precipitation distributions. While the Taiwan gauge network

is relatively dense (~1 gauge per 40 km^2), some local maxima could still miss the gauge sites due to highly variable precipitation distributions. The gauge-corrected radar QPE (Fig. 14c) mitigated overestimations (dashed cyan circle) in the radar-only QPE due to clutter contamination while retaining a finescale rainband structure in the typhoon (solid cyan circle). The gauge-corrected radar QPE provides more coverage over ocean than the gauge-only QPE, which can be useful for recreational industry and fisheries.

The LGC product is widely used by various government agencies and emergency managers for their decision making support. For instance, the SWCB uses the product to calculate a

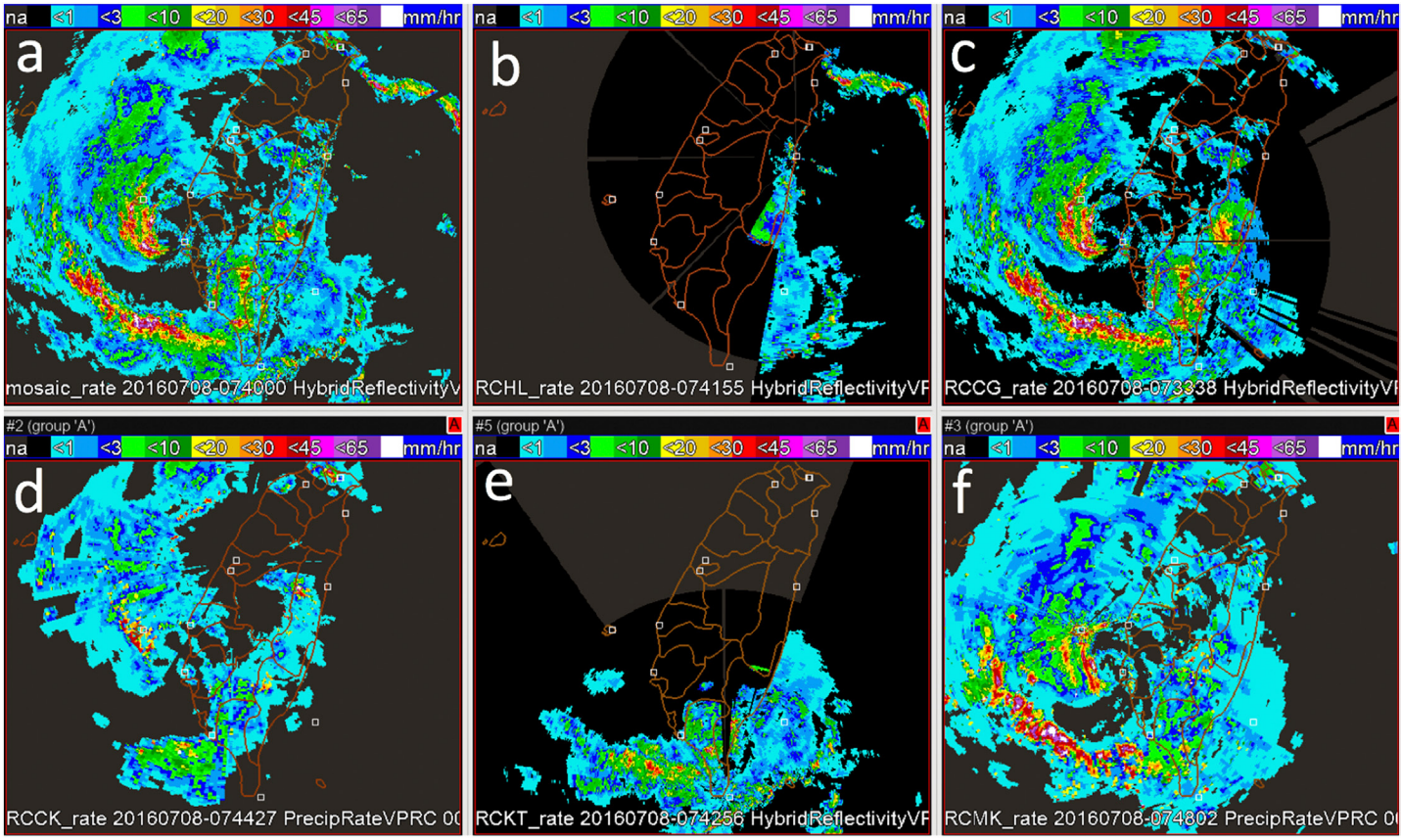

Fig. 13. Example (a) mosaicked and individual radar precipitation rate fields from (b) RCHL, (c) RCCG, (d) RCCK, (e) RCKT, and (f) RCMK at ~0740 UTC 8 Jul 2016.

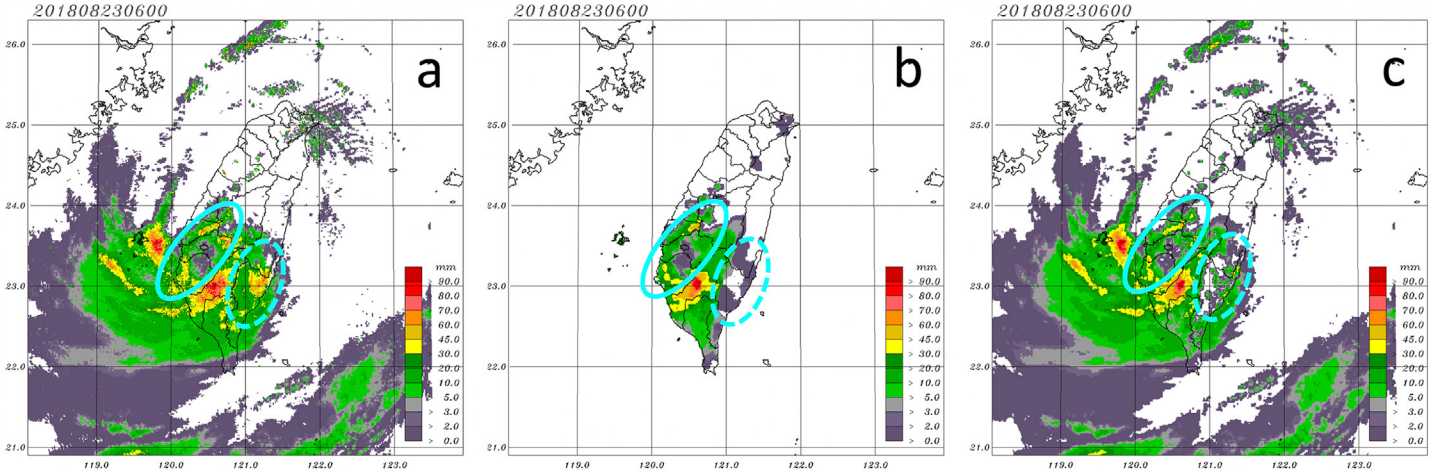

Fig. 14. Example hourly (a) radar-only, (b) gauge-only, and (c) the local gauge-corrected radar QPEs ending at 0600 UTC 23 Aug 2018. The solid cyan circle indicates a narrow rainband and dashed cyan circle an area of ground clutter contamination.

7-day running effective rainfall (Tsai et al. 2014) to help their issuance of debris flow alerts. The WRA uses the product as a forcing to their hydrological predictions, which are essential for their operational flash floods and river level warnings, flood routing, and reservoir discharging management.

Evaluations

The Taiwan QPESUMS radar QPE products were evaluated against gauge observations at hourly and daily scales for 2017–18. Figure 15 shows box-and-whisker plots of four statistic scores of the daily radar QPE, i.e., mean bias ratio (MBR), correlation coefficient (CC), mean absolute error (MAE), and the fractional MAE (fMAE). The four scores are defined as follows:

$$\mathrm{MBR} = \overline{Q}/\overline{G}, \tag{12}$$

$$\overline{Q} = \frac{\sum_{i=1}^{N} Q_i}{N}, \tag{13a}$$

$$\overline{G} = \frac{\sum_{i=1}^{N} G_i}{N}, \tag{13b}$$

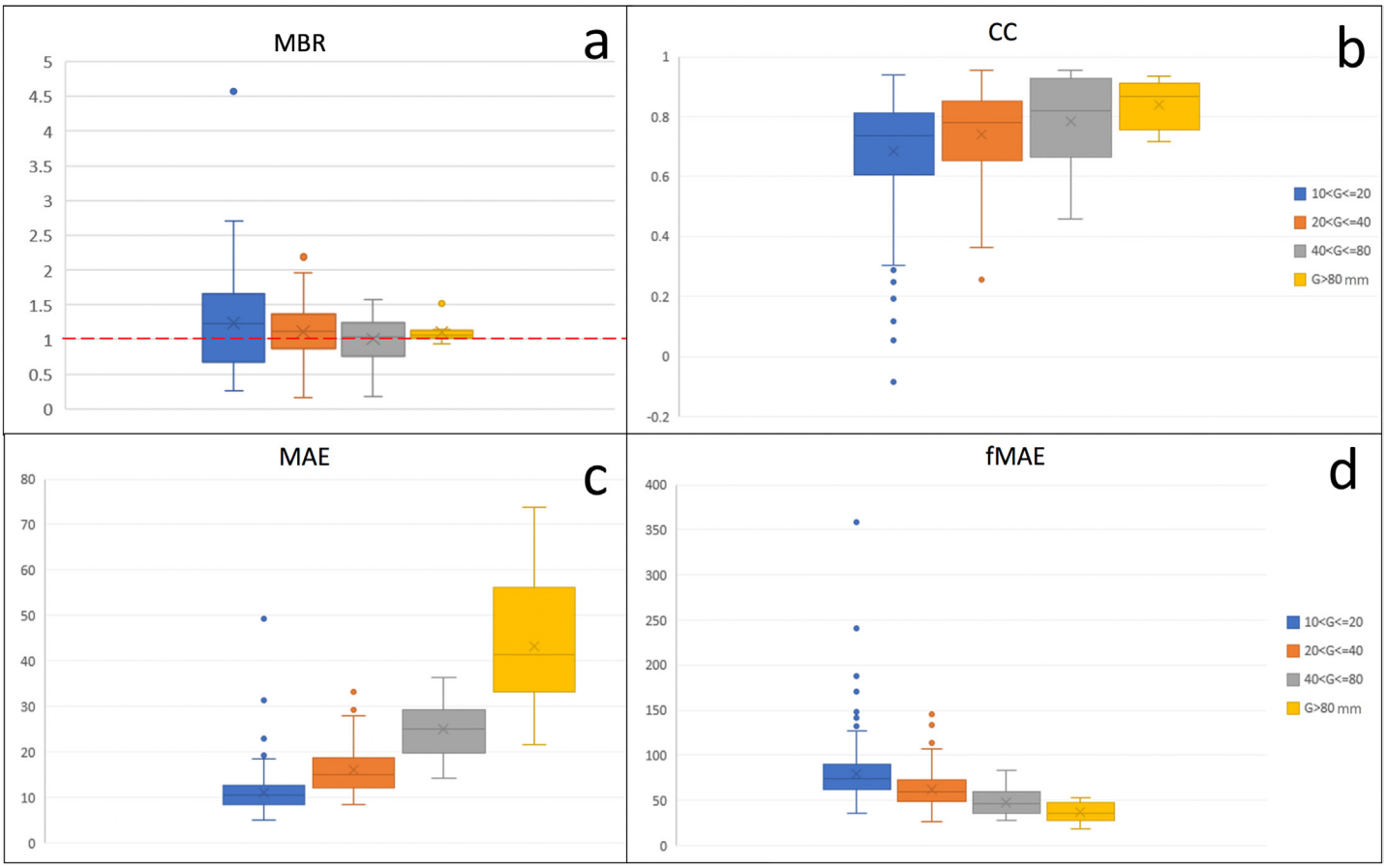

Fig. 15. Box-and-whisker plots of the (a) mean bias ratio (MBR), (b) correlation coefficient (CC), (c) mean absolute error (MAE), and (d) fractional MAE (fMAE) of the daily radar QPE vs gauges for 2017 and 2018.

$$\mathrm{CC} = \frac{\sum_{i=1}^{N}\left(Q_i - \bar{Q}\right)\left(G_i - \bar{G}\right)}{\sqrt{\sum_{i=1}^{N}\left(Q_i - \bar{Q}\right)^2 \sum_{i=1}^{N}\left(G_i - \bar{G}\right)^2}}, \tag{14}$$

$$\mathrm{MAE} = \frac{1}{N}\sum_{i=1}^{N}\left|Q_i - G_i\right|, \tag{15}$$

$$\mathrm{fMAE} = 100 \times \mathrm{MAE}/\bar{G}. \tag{16}$$

Here G_i is the 24-h rainfall observation by the ith gauge, Q_i is the collocated 24-h radar QPE, and N is the total number of gauges for a given data group. The scores are calculated for four data groups with different daily rainfall amounts (i.e., 10–20, 20–40, 40–80, and greater than 80 mm; Fig. 15). The daily radar QPE showed a ~20% overestimation bias (Fig. 15a) for the amounts between 10 and 20 mm and ~10% overestimation bias between 20 and 40 mm. No apparent bias was found for the higher amounts. The radar QPE had better correlation (Fig. 15b) with the gauges for the higher amounts than the lower amounts. While the MAE (Fig. 15c) was higher for the higher amounts, the relative error (fMAE, Fig. 15d) was smaller. Overall, the radar QPE performed better for heavier daily rainfall over 80 mm with less systematic bias and random errors. The lower uncertainty of the radar QPE at higher amounts was beneficial to the CWB and other government agencies' operations since heavy rainfall is the main driver for river floods and mudslides.

The radar QPE was further evaluated on an hourly scale to better understand the contributing factors to the various errors. Figure 16a shows a scatterplot of the hourly radar QPE versus gauges for 585 h of widespread heavy rainfall. The widespread heavy rainfall was defined as the ±3-h window of the hours when 1) the area of 1 mm or higher rainfall was greater than 40% of the QPESUMS domain; 2) the area of 40 mm or higher rainfall was greater than 1%

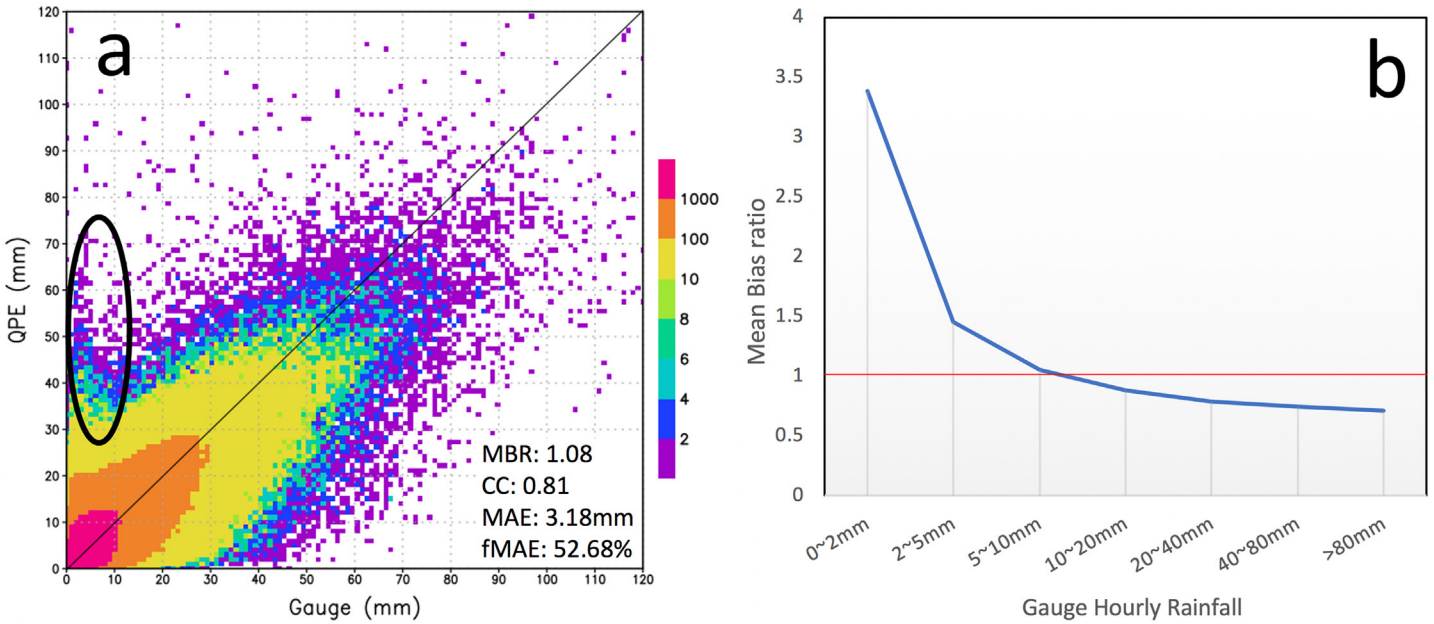

Fig. 16. (a) Scatterplot of the hourly radar QPE vs gauges for 585 h of widespread heavy rain periods in 2017 and 2018. (b) The categorized MBRs.

of the domain; and 3) the conditions 1) and 2) lasted for at least 2 h. The overall MBR for the hourly QPEs was 1.08 and CC was 0.81. Similar to the daily QPE, there was an apparent overestimation for the lighter amounts (<5 mm, Fig. 16b). However, for the higher hourly rainfalls (>20 mm), there were underestimation biases (Fig. 16b). One contributing factor to the overestimation at the lower amounts was the contamination of residual ground clutter after the QC, which was reflected by a cluster of radar QPEs over 30 mm for gauge rainfall below 10 mm (black circle, Fig. 16a). Identification of such clutter was a challenge for the single-pol radar QC because of the limited radar variables and the similar reflectivity characteristics between the clutter and precipitation echoes (e.g., Fig. 6a). A refined radar data QC based on multivariable fuzzy logic is currently under testing and is expected to further mitigate such contamination. Upgrade of the single-pol radars to dual-pol capabilities will significantly reduce these ground clutter. Another contributing factor to the overestimation at the lower amounts was the uncertainties associated with the $R(Z)$ relationship for the S-band single-pol radars. While the current $R(Z)$ relationship yields unbiased QPE for relatively heavy tropical rain (e.g., in typhoons), it tends to overestimate for light and continental type rain. The dual-pol upgrade will likely mitigate such uncertainties associated with $R(Z)$ and provide a more accurate QPE (e.g., Figs. 11 and 12).

The underestimation bias at the higher amounts was associated with two main factors: 1) degraded radar coverage in the complex terrain and 2) uncertainties in the $R(Z)$ relationship. To understand the impact of the complex terrain, the hourly radar QPE was divided into two groups, one for the plain areas with an elevation ≤ 500 m above MSL and another the mountain areas with an elevation > 500 m above MSL. For both groups, the contamination of residual ground clutter (black circles, Figs. 17a and 17b) and the trend of overestimation at the lower amounts were apparent (Fig. 17c). For plain areas, the radar QPE correlated with the gauge observations very well (CC = 0.85) with an MBR of 1.15. For mountainous areas, the MBR was lower (0.95 vs 1.15) but the fMAE was larger (56.07% vs 50.94%). The underestimation bias for hourly rainfalls of 10 mm or greater was more significant in the mountainous areas than in the plains (Fig. 17c). Such underestimation bias was largely related to radar blockage in the complex terrain (Figs. 8 and 13). The severe blockage forced the radar QPE to use data from higher tilts that sometimes overshoot the precipitation processes near the ground. Since significant coalescence growth may occur in the lower part of precipitation systems that are orographically forced in a moist environment, radar QPE derived from the higher tilts could miss the growth and result in an underestimation. Further, different heavy rainfall regimes may have different DSDs. One single $R(Z)$ relationship cannot accurately capture the liquid water content everywhere due to the highly nonlinear relationships between the two.

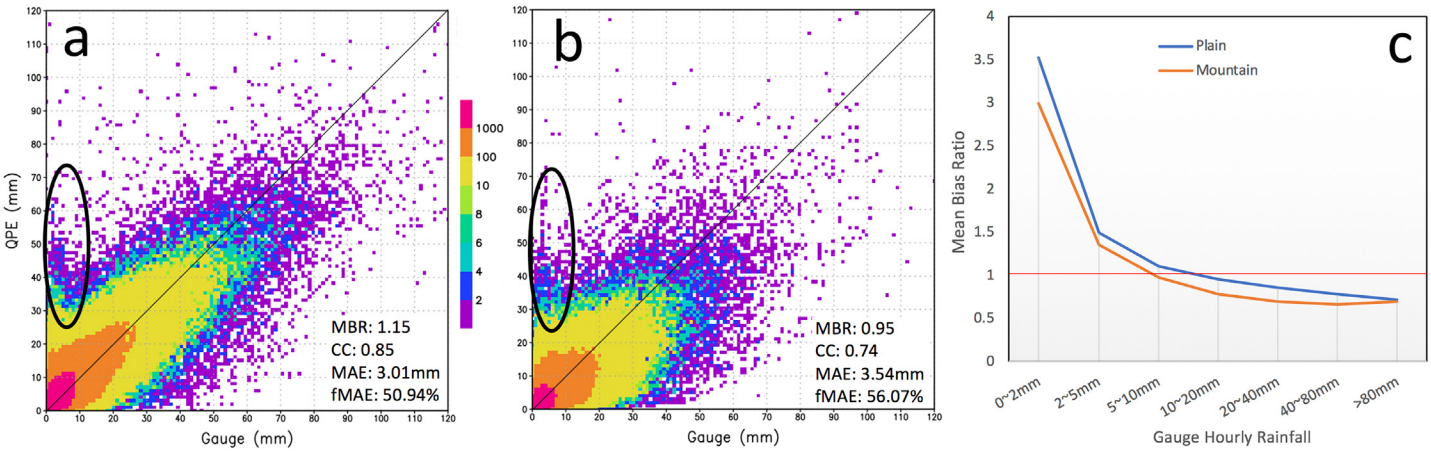

Fig. 17. As in Fig. 16, but segregated for the (a) plain and (b) mountain areas. (c) The categorized MBRs for the two areas.

Several ongoing efforts at CWB will potentially mitigate these over- and underestimation biases:

1) A multi-$R(Z)$ hybrid scheme is under development based on rainfall intensities, atmospheric environment, and geographical regions. The $R(Z)$ relationships will be derived from a new disdrometer network that consists of 27 stations across Taiwan. While $R(Z)$ relationships can be derived from collocated radar reflectivities and gauge data, such relationships may be skewed by factors that affect the representativeness of radar reflectivities (e.g., size of the radar sample volume, height of the data above the ground, potential calibration, and attenuation issues). The disdrometer network is helpful in providing independent $R(Z)$ relationships free of the radar calibration and sampling issues. The independent $R(Z)$ relationships are also important for obtaining accurate radar QPEs over the ocean where no gauges are available to correct for the radar QPE. Further, the in situ drop size distribution data may provide useful insights into the microphysical processes and benefit the NWP model community.
2) The additional C-pol radars will provide more low-level coverage and the C-pol QPE using $R(Z) + R(K_{DP})$ will improve the rainfall estimation accuracy in those areas as demonstrated in Figs. 11 and 12.
3) The single-pol S-band radars will be upgraded to dual-pol and the $R(Z)$ QPE will be replaced by $R(A)$, which provides more accurate QPEs than $R(Z)$ because of its insensitivities to calibration bias, attenuation, and partial blockages (e.g., Ryzhkov et al. 2014; Cocks et al. 2019; Zhang et al. 2020).

Summary and outlook

An operational multi-radar multi-sensor QPE system was developed in Taiwan as a result of the collaboration between the Taiwan Central Weather Bureau and NOAA's National Severe Storms Laboratory. The system integrates radar, gauge, and numerical weather prediction model data and generates high-resolution (1 km, 10 min) QPE products including the instantaneous rate and 1–72-h accumulations. A significant part of the system is the QC of data from a network of S-band single-pol, S-band dual-pol, and C-band dual-pol radars. In addition, each radar type has its own QPE scheme to derive precipitation rate from the quality-controlled radar data. The precipitation rate fields from each individual radar are mosaicked to generate an instantaneous precipitation rate field for the whole Taiwan domain. The rate field was aggregated into an hourly radar QPE every 10 min and then a local gauge correction (LGC) was applied to the hourly radar QPE. Finally, two suites of precipitation accumulation products are generated, one from the hourly radar QPE and another from the hourly LGC QPE. Each suite consists of 3–72-h accumulations updated every 10 min. Customized QPE products for local geographical and geopolitical areas (e.g., drainage basin, debris catchment basin, county) were also generated. The high-resolution and rapid update QPE products have been used for severe weather and flash flood situational awareness (Central Weather Bureau), river flood predictions (Water Resources Agency), mudslide monitoring (Soil and Water Conservation Bureau), and weather hazard warning decision support (local government emergency managers).

Future work will include the deployment of additional C-band dual-pol radars (Fig. 1). The three S-band single-pol radars, RCCG, RCHL, and RCKT, will be upgraded to dual-pol capabilities in the next 3 years. The upgrade will mark the completion of a dual-pol radar network with four S-band and eight C-band radars in Taiwan and will greatly improve the quality of the radar QPE. Several radar data QC improvements will be developed including the removal of electronic interference noises using a fuzzy logic technique. A machine learning QPE is currently under development and is expected to optimally blend multi-sensor data from

radar, numerical weather prediction model and satellite and to provide further improvement especially in areas of severe radar blockages.

Acknowledgments. This work was largely supported by the Taiwan Central Weather Bureau, Water Resources Agency, and Soil and Water Conservation Bureau and the funding was provided through the NOAA/Office of Oceanic and Atmospheric Research under NOAA–University of Oklahoma Cooperative Agreement NA11OAR4320072, U.S. Department of Commerce.

References

Bringi, V., V. Chandrasekar, N. Balakrishnan, and D. S. Zrnić, 1990: An examination of propagation effects in rainfall on radar measurements at microwave frequencies. *J. Atmos. Oceanic Technol.*, **7**, 829–840, https://doi.org/10.1175/1520-0426(1990)007<0829:AEOPEI>2.0.CO;2.

Chang, P.-L., P.-F. Lin, B. J.-D. Jou, and J. Zhang, 2009: An application of reflectivity climatology in constructing radar hybrid scans over complex terrains. *J. Atmos. Oceanic Technol.*, **26**, 1315–1327, https://doi.org/10.1175/2009JTECHA1162.1.

Chang, W.-Y., T.-C. C. Wang, and P.-L. Lin, 2009: Characteristics of the raindrop size distribution and drop shape relation in typhoon systems in the western Pacific from the 2D video disdrometer and NCU C-band polarimetric radar. *J. Atmos. Oceanic Technol.*, **26**, 1973–1993, https://doi.org/10.1175/2009JTECHA1236.1.

Chen, I.-H., J.-S. Hong, Y.-T. Tsai, and C.-T. Fong, 2020: Improving afternoon thunderstorm prediction over Taiwan through 3DVar-based radar and surface data assimilation. *Wea. Forecasting*, **35**, 2603–2620, https://doi.org/10.1175/WAF-D-20-0037.1.

Chen, J.-Y., W.-Y. Chang, and T.-C. Chen, 2017: Comparison of quantitative precipitation estimation in northern Taiwan using S- and C-band dual-polarimetric radars (in Chinese). *Atmosphere*, **45**, 57–80, https://doi.org/10.3966/025400022017034501004.

Ching, J., H.-J. Liao, and J.-Y. Lee, 2011: Predicting rainfall-induced landslide potential along a mountain road in Taiwan. *Geotechnique*, **61**, 153–166, https://doi.org/10.1680/geot.8.P.119.3740.

Cocks, S., and Coauthors, 2019: A prototype quantitative precipitation estimation algorithm for operational S-Band polarimetric radar utilizing specific attenuation and specific differential phase. Part II: Performance verification and case study analysis. *J. Hydrometeor.*, **20**, 999–1014, https://doi.org/10.1175/JHM-D-18-0070.1.

Germann, U., G. Galli, M. Boscacci, and M. Bolliger, 2006: Radar precipitation measurement in a mountainous region. *Quart. J. Roy. Meteor. Soc.*, **132**, 1669–1692, https://doi.org/10.1256/qj.05.190.

Giangrande, S. E., and A. V. Ryzhkov, 2008: Estimation of rainfall based on the results of polarimetric echo classification. *J. Appl. Meteor. Climatol.*, **47**, 2445–2462, https://doi.org/10.1175/2008JAMC1753.1.

Gourley, J. J., and Coauthors, 2017: The FLASH project: Improving the tools for flash flood monitoring and prediction across the United States. *Bull. Amer. Meteor. Soc.*, **98**, 361–372, https://doi.org/10.1175/BAMS-D-15-00247.1.

IFRC, 2018: Leaving no one behind: World Disasters Report 2018. International Federation of Red Cross and Red Crescent Societies, 20 pp., https://media.ifrc.org/ifrc/wp-content/uploads/sites/5/2018/10/B-WDR-2018-EXECSUM-EN.pdf.

Jou, B.-J. D., Y.-C. Kao, R.-G. R. Hsiu, C.-J. U. Jung, J. R. Lee, and H.-C. Kuo, 2016: Observational characteristics and forecast challenge of Taipei flash flood afternoon thunderstorm: Case study of 14 June 2015 (in Chinese). *Atmos. Sci.*, **44**, 57–82.

Kuo, Y.-C., M.-A. Lee, and M.-M. Lu, 2016: Association of Taiwan's rainfall patterns with large-scale oceanic and atmospheric phenomena. *Adv. Meteor.*, **2016**, 3102895, https://doi.org/10.1155/2016/3102895.

Lakshmanan, V., A. Fritz, T. Smith, K. Hondl, and G. Stumpf, 2007: An automated technique to quality control radar reflectivity data. *J. Appl. Meteor. Climatol.*, **46**, 288–305, https://doi.org/10.1175/JAM2460.1.

——, J. Zhang, and K. Howard, 2010: A technique to censor biological echoes in radar reflectivity data. *J. Appl. Meteor. Climatol.*, **49**, 453–462, https://doi.org/10.1175/2009JAMC2255.1.

Liu, Z., J. Ban, J.-S. Hong, and Y.-H. Kuo, 2020: Multi-resolution incremental 4DVar for WRF: Implementation and application at convective scale. *Quart. J. Roy. Meteor. Soc.*, https://doi.org/10.1002/qj.3865, **146**, 3661–3674, https://doi.org/10.1002/qj.3865.

Meymaris, G., M. J. Dixon, S. M. Ellis, and J. C. Hubbert, 2015: Clutter Mitigation Decision (CMD) development and evaluation using neural networks. *37th Conf. on Radar Meteorology*, Norman, OK, Amer. Meteor. Soc., 2B.3A, https://ams.confex.com/ams/37RADAR/webprogram/Paper276333.html.

Nguyen, C. M., and V. Chandrasekar, 2013: Gaussian model adaptive processing in time domain (GMAP-TD) for weather radars. *J. Atmos. Oceanic Technol.*, **30**, 2571–2584, https://doi.org/10.1175/JTECH-D-12-00215.1.

Park, H. S., A. V. Ryzhkov, D. S. Zrnić, and K.-E. Kim, 2009: The hydrometeor classification algorithm for the polarimetric WSR-88D: Description and application to an MCS. *Wea. Forecasting*, **24**, 730–748, https://doi.org/10.1175/2008WAF2222205.1.

Ryzhkov, Z., M. Diederich, P. Zhang, and C. Simmer, 2014: Potential utilization of specific attenuation for rainfall estimation, mitigation of partial beam blockage, and radar networking. *J. Atmos. Oceanic Technol.*, **31**, 599–619, https://doi.org/10.1175/JTECH-D-13-00038.1.

Siggia, A. D., and R. E. Passarelli, 2004: Gaussian model adaptive processing (GMAP) for improved ground clutter cancellation and moment calculation. *Proc. Third European Conf. on Radar Meteorology (ERAD)*, Visby, Sweden, ERAD, 67–73, www.copernicus.org/erad/2004/online/ERAD04_P_67.pdf.

Sun, J., Y. Zhang, J. Ban, J.-S. Hong, and C. Lin, 2020: Impact of combined assimilation of radar and rainfall data on short-term heavy rainfall prediction: A case study. *Mon. Wea. Rev.*, **148**, 2211–2232, https://doi.org/10.1175/MWR-D-19-0337.1.

Tabary, P., 2007: The New French operational radar rainfall product. Part I: Methodology. *Wea. Forecasting*, **22**, 393–408, https://doi.org/10.1175/WAF1004.1.

Tang, B., J. Tang, and Y. Peng, 2012: Detection of heterogeneous samples based on loaded generalized inner product method. *Digital Signal Process.*, **22**, 605–613, https://doi.org/10.1016/j.dsp.2012.03.001.

Tang, L., J. Zhang, C. Langston, J. Krause, K. Howard, and V. Lakshmanan, 2014: A physically based precipitation–nonprecipitation radar echo classifier using polarimetric radar and environmental data in a real-time system. *Wea. Forecasting*, **29**, 1106–1119, https://doi.org/10.1175/WAF-D-13-00072.1.

Testud, J., E. L. Bouar, E. Obligis, and M. Ali-Mehenni, 2000: The rain profiling algorithm applied to polarimetric weather radar. *J. Atmos. Oceanic Technol.*, **17**, 332–356, https://doi.org/10.1175/1520-0426(2000)017<0332:TRPAAT>2.0.CO;2.

Tsai, M., Y. M. Huang, Y. Fang, B. J. Lee, T. Y. Chou, and H. Yin, 2014: Characteristics of debris flow in Taiwan – A case study in Shenmu Area. *INTERPRAEVENT Int. Symp.*, Nara, Japan, INTERPRAEVENT International Research Society, 117–125, www.interpraevent.at/palm-cms/upload_files/Publikationen/Tagungsbeitraege/2014_1_117.pdf.

Vivekanandan, J., G. Zhang, S. M. Ellis, D. Rajopadhyaya, and S. K. Avery, 2003: Radar reflectivity calibration using differential propagation phase measurement. *Radio Sci.*, **38**, 8049, https://doi.org/10.1029/2002RS002676.

Wang, Y., J. Zhang, B. Kaney, C. Langston and K. Howard, 2012: High-Resolution Quantitative Precipitation Estimation and Quantitative Precipitation Forecast (HRQ2) System. Final Rep. for the International Agreement #24 between NOAA and the American Institute in Taiwan for Technical Cooperation in Meteorology and Forecast Systems Development, 64 pp.

——, ——, A. Ryzhkov, and L. Tang, 2013: C-Band polarimetric radar QPE based on specific differential propagation phase for extreme typhoon rainfall. *J. Atmos. Oceanic Technol.*, **30**, 1354–1370, https://doi.org/10.1175/JTECH-D-12-00083.1.

——, ——, P.-L. Chang, C. Langston, B. Kaney and L. Tang, 2016: Operational C-Band dual-polarization radar QPE for the subtropical complex terrain of Taiwan. *Adv. Meteor.*, **2016**, 4294271, https://doi.org/10.1155/2016/4294271.

——, S. Cocks, L. Tang, A. Ryzhkov, P. Zhang, J. Zhang, and K. Howard, 2019: A prototype quantitative precipitation estimation algorithm for operational S-band polarimetric radar utilizing specific attenuation and specific differential phase. Part I: Algorithm description. *J. Hydrometeor.*, **20**, 985–997, https://doi.org/10.1175/JHM-D-18-0071.1.

Xie, Y. F., S. Koch, J. McGinley, S. Albers, P. Beringer, M. Wolfson, and M. Chan, 2011: A space–time multiscale analysis system: A sequential variational analysis approach. *Mon. Wea. Rev.*, **139**, 1224–1240, https://doi.org/10.1175/2010MWR3338.1.

Xin, L., G. Recuter, and B. Larochelle, 1997: Reflectivity-rain rate relationship for convective rainshowers in Edmonton: Research note. *Atmos.–Ocean*, **35**, 513–521, https://doi.org/10.1080/07055900.1997.9649602.

Zhang, J., and Coauthors, 2008: High-resolution QPE system for Taiwan. *Data Assimilation for Atmospheric, Oceanic, and Hydrologic Applications*, S. K. Park and L. Xu, Eds., Springer-Verlag, 147–162.

——, and Coauthors, 2011: National mosaic and multi-sensor QPE (NMQ) system: Description, results and future plans. *Bull. Amer. Meteor. Soc.*, **92**, 1321–1338, https://doi.org/10.1175/2011BAMS-D-11-00047.1.

——, and Coauthors, 2016: Multi-Radar Multi-Sensor (MRMS) quantitative precipitation estimation: Initial operating capabilities. *Bull. Amer. Meteor. Soc.*, **97**, 621–638, https://doi.org/10.1175/BAMS-D-14-00174.1.

——, and Coauthors, 2020: A dual-polarization radar synthetic QPE for operations. *J. Hydrometeorol.*, **21**, 2507–2521.